https://doi.org/10.5194/egusphere-2026-977
Preprint. Discussion started: 19 March 2026

Aerodynamic evaluation of wind speed sensor placement on UAVs for meteorological applications

Ashish Pastay[1], Shrivathsan Narayanan[1], and Bharath Govindarajan[2]

[1]Department of Aerospace Engineering, Indian Institute of Technology Madras, Chennai, India
[2]Department of Aerospace Engineering, Indian Institute of Technology Madras; also at the Geophysical Flows Lab, Center of Excellence, Chennai, India

Correspondence: Ashish Pastay (ashishpastay18@gmail.com)

Abstract.

Vertical takeoff and landing Unmanned Aerial Vehicles (VTOL-UAVs) can provide accurate, highly resolved, and repeatable atmosphere measurements, especially in scenarios where conventional measurement techniques are inadequate, or impractical. Wind estimation using UAV-mounted sensors is significantly influenced and contaminated by rotor-induced flows, making its placement a critical design consideration for meteorological measurements. This work investigates optimal locations for wind speed sensor placement on various UAV systems by studying the rotor-induced flow field using a free-vortex wake model (FVM) across a single-rotor, quad-rotor, and hexa-rotor configurations under hover, axial descent, and forward-descent flight conditions. This model is validated with an in-house experimental setup for velocity measurements. Care is taken to ensure these results are applicable across a wide range of practical UAV operating conditions through the dimensional disk loading (DL) parameter. The rotor-induced velocity fields are evaluated on multiple planes perpendicular to the rotor disk, and "quiet-zones" for sensor placement are identified based on a threshold of 1% rotor-tip speed. Results reveal that the location and extent of the quiet-zones are strongly dependent on the flight condition. For single-rotor in hover, a well-defined quiet-zone exists above the rotor disk, while viable sensor placement locations are substantially reduced in axial descent. Forward descent introduces asymmetric wake skew, limiting quiet-zones to the upstream, at smaller axial distances. For multi-rotor configurations, the system geometric center is particularly suitable for sensor placement, compared to axial locations about the individual rotor hubs. Overall, by analyzing various rotor systems in different flight conditions, the present work provides a practical guidance for the design of accurate UAV-based atmospheric measurement systems.

Keywords. Wind measurement, Sensor placement, Unmanned Aerial Vehicles, Multi-rotor Aerodynamics, Free Vortex Method

https://doi.org/10.5194/egusphere-2026-977
Preprint. Discussion started: 19 March 2026

1 Introduction

Detection of wind is of paramount importance to our understanding of atmospheric dynamics, weather forecasting, climate monitoring, dispersion of contaminants and other allied phenomena, and applications. Meticulous observations of wind phenomena are particularly vital in inaccessible or data-scarce regions, where conventional observation methods fail to provide high accuracy wind data. Figure 1 shows a schematic of conventional wind sensing strategies and the typical altitudes where they are most effective. Traditionally used platforms such as weather balloons (Fujiwara et al., 2025) together with a radiosonde (Faber et al., 2023) are single-use and drift considerably with the wind, making it nearly impossible to obtain controlled and repeatable wind profile trajectories. Additionally, the wind-velocity and direction estimated by these balloons may not be sensitive to high-frequency changes in the wind, because of the system's inertia and the consequent drifting of the balloon system. Aircraft-based observations (Gasch et al., 2023) are expensive and require significant infrastructure, making them less ideal for routine deployments in isolated or hazardous areas. Ground-based radar systems and profiling stations (Ritvanen et al., 2022) offer high-fidelity data but demand substantial investment; and these radar systems are also limited to land regions, rendering them ineffective over oceans or even remote mountainous terrains. Satellite-based wind sensing is effective over the upper regions of the atmosphere, but is sensitive to cloud cover (Stoffelen et al., 2005), which limits the spatial and temporal resolutions of the collected data. Furthermore, the data gathered depend on the trajectory of the satellite and the local atmospheric conditions.

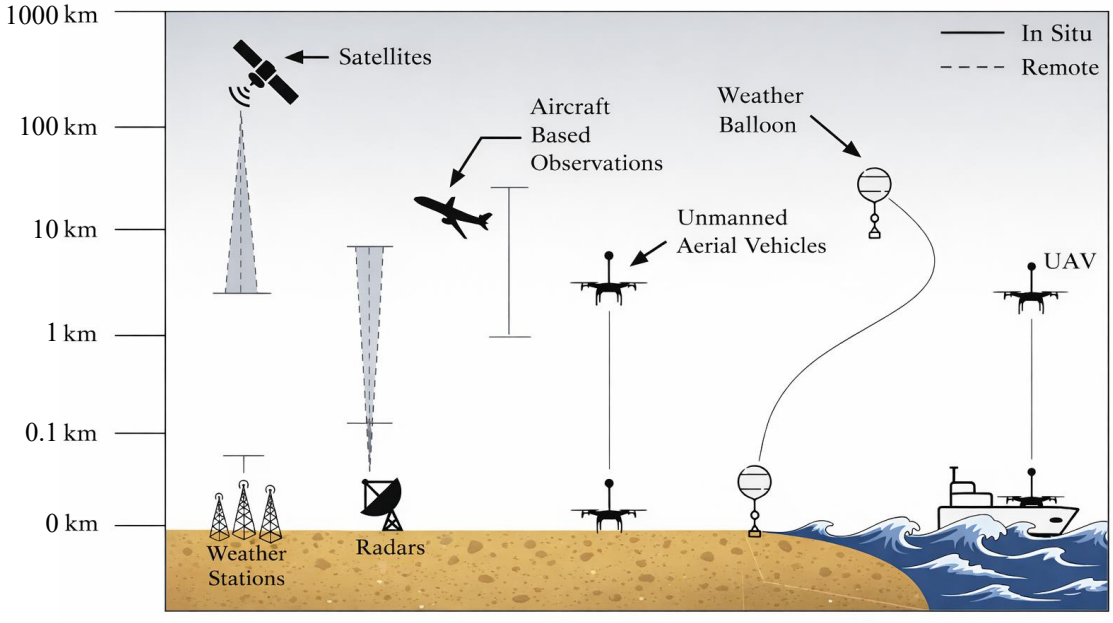

Figure 1. Conventional atmospheric sensing platforms and the potential role of UAVs.

https://doi.org/10.5194/egusphere-2026-977
Preprint. Discussion started: 19 March 2026

In contrast, Unmanned Aerial Vehicles (UAVs, or drones) are a versatile and affordable option when used for in situ wind sensing. UAVs have been gaining attention in the meteorological and atmospheric measurement space, particularly for wind speed and direction measurements, wind profiling in the atmospheric boundary layer (ABL), and small-scale turbulence measurements (Thielicke et al., 2021; Hollenbeck et al., 2018; Jin et al., 2024; Ghirardelli et al., 2025). Because of their lower cost compared to other strategies and relatively smaller size, they can be deployed repeatedly and selectively to measure the desired wind profiles. They can accommodate mission-specific requirements, can be programmed to follow controlled trajectories, and can carry out high-resolution wind profiling at user-specified altitudes. These merits of UAVs can complement conventional atmospheric sensing platforms, wherever the latter is not effective or unable to obtain valid measurements. Of the many atmospheric science questions that remain unanswered, understanding of the various phenomena prevalent in the ABL, i.e., within 5 km above mean sea level (Witte et al., 2017), still remains one of the most important frontiers in the domain of meteorological studies; and the ability of UAVs to obtain atmospheric data within the ABL presents them as a potential candidate to bridge current observational gaps and improve data coverage in remote environments.

A key question that arises in using UAVs to carry out measurements of wind velocity and direction is the placement of a wind-speed sensor, particularly in configurations that feature rotors/propellers. It is known that these rotary wing systems entrain the flow around them and there is a velocity field that develops in the vicinity of the rotor (Leishman, 2006a). The nature of these flow fields, i.e., the magnitude of velocity and its “hotspots" relative to the rotor/propeller, is dependent on the size of the rotors, the thrust they generate, and the flight condition. On one hand, if the wind-speed sensor is placed significantly close to the rotors, it is affected by the complicated aerodynamic environment surrounding the system, particularly the flow that is entrained through the rotor disk which would corrupt the wind signals. However, if the sensor is placed considerably far away from the rotors, it is no longer affected by the flow around the rotor; but the inertia of the system shifts towards the sensor, leading to poor vehicle stability and handling concerns during flight. Such issues only amplify and create additional challenges in unsteady or gusty conditions. Therefore, perhaps there exists an optimal location of the wind-sensor placement that allows for accurate measurement of the wind while maintaining sufficient control authority of the UAV. The present work focuses only on the aerodynamics of the problem and does not provide a detailed account of the controls aspect.

Figure 2 shows the various types of UAV-mountable wind speed sensors based on different measurement principles. The pitot-static tube (Fig. 2a) is used to measure airspeed from the pressure difference between its stagnation and static ports; pitot-tubes can be used to approximate the wind vector if combined with the ground speed obtained from GPS systems (Cho et al., 2011). The mechanical cup anemometer (Fig. 2b) is a wind speed measurement system based on the rotational speed of a set of hemispherical cups that rotate at a rate proportional to the wind velocity; The cup anemometer is typically calibrated by magnetic or optical encoders (Pindado et al., 2014). The thermal (hot-film) anemometer (Fig. 2c) determines the flow velocity from the cooling rate of a heated filament exposed to the flow. The voltage supplied to the filament is adjusted to maintain a steady temperature, and the flow velocity is calculated using a calibration procedure; the hot-film anemometer is highly effective when measuring the wind velocity in turbulent flow, but the sensor does not inherently indicate the flow direction (Simon et al., 2022; Inoue and Sato, 2022). The 3D ultrasonic anemometer (Fig. 2d) measures wind velocity magnitude and direction by determining the transit-time differences of ultrasonic pulses between transducers. All components of velocity can be directly

https://doi.org/10.5194/egusphere-2026-977
Preprint. Discussion started: 19 March 2026

(a) (b) (c) (d)

Figure 2. Representative UAV-mountable wind sensors based on different measurement principles: **(a)** Pitot–static tube, **(b)** Mechanical cup anemometer, **(c)** Thermal (hot-film) anemometer, and **(d)** 3D ultrasonic anemometer.

estimated with high temporal resolution and minimal flow disturbance, making it very suitable for accurate wind measurements on UAV platforms (Thielicke et al., 2021; Hollenbeck et al., 2018; Basawanal et al., 2025).

Recent investigations have been conducted into the placement of atmospheric sensors for UAV-based measurements that examine the influence of propeller-induced flow; however, the general body of literature remains limited. Wilson et al. (2022) combined laboratory Particle Image Velocimetry (PIV) measurements with field experiments on a quadcopter platform to characterize rotor-induced velocities above the UAV. It was shown that placing sensors approximately 5.3 rotor diameters above the rotor plane yields wind speed measurements that closely match mast-mounted references, with differences within 5.5% and preserved spectral characteristics. Ghirardelli et al. (2023) quantified propeller-induced flow effects on UAV-mounted wind sensors using normalized wind speed deviation metrics in a Computational Fluid Dynamics (CFD) study of a coaxial multicopter. For the specific platform utilized in the study, regions of minimal flow disturbance were identified upstream and below the rotor plane, corresponding to horizontal and vertical offsets of approximately 0.46–1.66 and 0.01–0.70 rotor diameters, respectively. Thielicke et al. (2021) developed a custom rotary-wing UAV equipped with a full-scale ultrasonic anemometer and validated its performance through calibration wind-tunnel experiments, large-scale wind-tunnel tests with operating rotors, and field comparisons against bistatic Doppler LiDAR. Wind velocity was reconstructed as the total wind vector using data fusion of measured relative velocity and UAV kinematics. The propeller-induced effects were explicitly isolated and corrected for the UAV platform considered in the study, and a negligible influence on horizontal velocity was observed when the sensor was mounted approximately 2.5 rotor diameters above the rotor plane. However, the study does not provide a generalized or scalable framework for predicting propeller-induced effects or optimizing sensor placement across different multi-rotor geometries and operating conditions. In another study, Jin et al. (2024) employed Reynolds-averaged CFD validated using tri-beam Doppler LiDAR measurements to quantify propeller-induced effects through normalized deviations of horizontal wind speed relative to freestream velocity. Their analysis showed that the regions of minimum flow distortion are located upstream of the UAV and below the rotor plane. Under a stringent disturbance criterion of 1% of velocity, the vertical wind component remained affected even at an upstream separation distance of approximately 5 m (about 7 rotor diameters), corresponding to a boom length that is impractical for a multi-copter with a rotor diameter of 0.71 m and an overall

https://doi.org/10.5194/egusphere-2026-977
Preprint. Discussion started: 19 March 2026

span of 1.88 m. When a less restrictive threshold of 5% velocity deviation was adopted, the required upstream separation reduced to approximately 2 m at ambient wind speeds exceeding 4 $\mathrm{m\,s^{-1}}$. More recently, Ghirardelli et al. (2025) presented the SAMURAI-S system, in which a research-grade ultrasonic anemometer is suspended as a sling load of approximately 18 m ($\sim$ 26 rotor diameters) below a multi-rotor UAV to completely eliminate propeller-induced effects. While this configuration enables accurate measurements of total wind and turbulence, the sensor was intentionally positioned far from the UAV frame and therefore does not inform practical near-body sensor placement strategies for compact multi-rotor platforms.

Collectively, these studies demonstrate the importance of understanding rotor wake characteristics for appropriate sensor placement; however, the reliance on expensive computational and/or experimental infrastructure limits their applicability to multi-rotor configurations and large parametric studies. Furthermore, although commercial UAV-based atmospheric measurement platforms are available (Menapia Ltd., 2025; Meteomatics AG, 2025), detailed and publicly available information regarding their wind sensor placement strategies remains scarce, underscoring the need for systematic and cost-effective investigation.

In summary, it is crucial to understand the aerodynamic disturbances generated by UAV rotors in their vicinity to fully exploit the potential of UAV mounted wind-speed sensors for meteorological applications. Identifying “low-disturbance zones" or “quiet-zones" around a UAV is of fundamental importance for optimal sensor placement and accurate wind measurement. The dearth of publicly available information on state-of-the art UAV wind measurement systems underscores the need for systematic studies to identify optimal sensor placement strategies that minimize the influence of rotor-induced flow. Although CFD studies in the literature have provided some insight, as a tool, CFD is computationally expensive to sweep through a wide variety of UAV configurations and operating conditions.

The focus of the present study is to use an alternate relatively parsimonious model (based on vortex methods), which presents the possibility of performing analyzes on a vast array of scenarios. Specifically, an in-house free-vortex wake model (FVM) is used to analyze the wake behavior of UAV-scale rotor systems under different flight and thrust conditions to identify optimal zones for wind sensor placement. The study is performed on an isolated rotor, a quad-rotor, and a hexa-rotor configuration of a UAV-scale propeller. To validate the wind speed measurements, a supporting experimental setup is also utilized. The setup employs an ultrasonic anemometer (TriSonica Mini wind and weather sensor, shown in Fig. 2d) for wind velocity measurements, chosen for its reliable low-speed response, high temporal resolution, and direct three-component velocity measurement with minimal flow distortion.

2 Methodology

2.1 Free-vortex wake model (FVM)

FVMs are a class of mid-fidelity numerical tools specifically tailored to simulating vortex-dominated flows and capture key rotorcraft flow field features. They lie between the traditional low-fidelity dynamic inflow models (Lee et al., 2022) and more expensive high-fidelity CFD approaches (Datta et al., 2005) to analyze the aerodynamics of rotor systems. FVMs offer a trade-off between solution accuracy and computational efficiency (Zanotti et al., 2021), making them suitable for analyzing complex multi-rotor configurations, involving large parameter sweeps. Furthermore, several flow field intricacies such as blade-vortex

https://doi.org/10.5194/egusphere-2026-977
Preprint. Discussion started: 19 March 2026

interactions are efficiently captured by FVMs (Romani and Casalino, 2019), adding to their credibility in solving unsteady rotorcraft aerodynamic problems. Furthermore, low-fidelity inflow models are not suitable for descent flight conditions (as they cannot capture the complex rotor-wake interactions), which are also of considerable interest in this study. The model developed by the authors for an earlier work (Narayanan and Govindarajan, 2024) has been utilized for the present study, and a few key parameters of the developed model are detailed below.

Governing equations: The governing equation for the FVM model is the velocity-vorticity form of the Navier-Stokes equation, which is solved under the assumption of potential flow (Bhagwat and Leishman, 2000; Leishman et al., 2002). The convection of free vortices is described by

$$\frac{d\boldsymbol{r}}{dt} = \boldsymbol{V}(\boldsymbol{r}) \tag{1}$$

where, $\boldsymbol{r}$ denotes the position vector of a point in the rotor wake, and $\boldsymbol{V}(\boldsymbol{r})$ represents the local fluid velocity at that point (Bhagwat and Leishman, 2000). Expressing the system in terms of the azimuthal position of the blade (ψ), the wake age (ζ) and the angular velocity of the rotor (Ω), the governing equation is reformulated as

$$\frac{\partial \boldsymbol{r}}{\partial \psi} + \frac{\partial \boldsymbol{r}}{\partial \zeta} = \frac{\boldsymbol{V}(\boldsymbol{r})}{\Omega} \tag{2}$$

Equation (2) is numerically solved using a second-order predictor-corrector (PC2B) method (Bhagwat and Leishman, 2000). Figure 3a presents a schematic representation of the FVM formulation adopted in this study. Each rotor blade is discretized

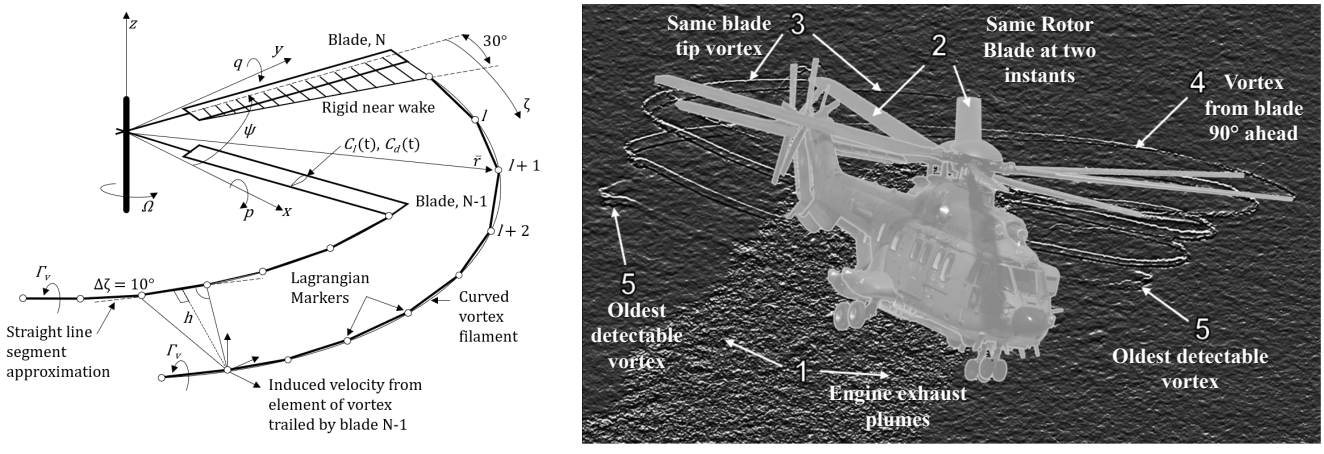

(a) (b)

Figure 3. Representative rotor wake structures in a typical rotorcraft aerodynamic environment: **(a)** Rotor blade discretization and near-wake structure used in the FVM model; **(b)** Helical blade-tip vortex wake structure of a Cougar helicopter visualized using the background-oriented schlieren (BOS) technique (adapted from Bauknecht et al., 2014 with permission).

https://doi.org/10.5194/egusphere-2026-977
Preprint. Discussion started: 19 March 2026

into 40 spanwise blade elements, and the unsteady aerodynamic loads on each element are computed using Blade Element Theory (BET), and a solution to the Duhamel integral (Leishman, 2006b), resulting in time-varying lift and drag coefficients $C_l(t)$ and $C_d(t)$. For all studies, a timestep equivalent to a 10° sweep of the blade is chosen, and at each timestep, changes in bound circulation are shed into the wake as free vortex filaments (Leishman et al., 2002). For numerical efficiency, the continuously curved wake is approximated using straight-line vortex segments generated over a 30° azimuthal interval (Bhagwat and Leishman, 2001). The wake is represented using Lagrangian markers, which denote the discrete spatial locations of the endpoints of the vortex filament and are convected in the Lagrangian framework under the local velocity field (Bhagwat and Leishman, 2000; Ananthan and Leishman, 2004). The typical wake structure beneath the rotor/ propeller is helical in nature as seen in Fig. 3b (Bauknecht et al., 2014) (adapted with permission), and consequently, in this study, six turns are retained.

Induced velocity calculations: Within the FVM formulation, the induced velocity at any point in space, at a given time step, is obtained by a vectorial summation of the contributions of all vortex filaments trailed into the rotor wake. This induced velocity $\boldsymbol{v}_i$ due to the vortex filament at a control point $\boldsymbol{r}$ is given according to the Biot-Savart law (Fig. 4a) as

$$\boldsymbol{v}_i(\boldsymbol{r}) = \frac{\Gamma}{4\pi} \int_{\text{filament}} \frac{d\boldsymbol{l} \times (\boldsymbol{r} - \boldsymbol{r}')}{|\boldsymbol{r} - \boldsymbol{r}'|^3} \tag{3}$$

where Γ denotes the strength of the vortex, $d\boldsymbol{l}$ is the elemental vortex segment, and $\boldsymbol{r}'$ represents the source point on the vortex filament. In the present formulation, the rotor wake vortices are discretized into finite straight-line segments, and the

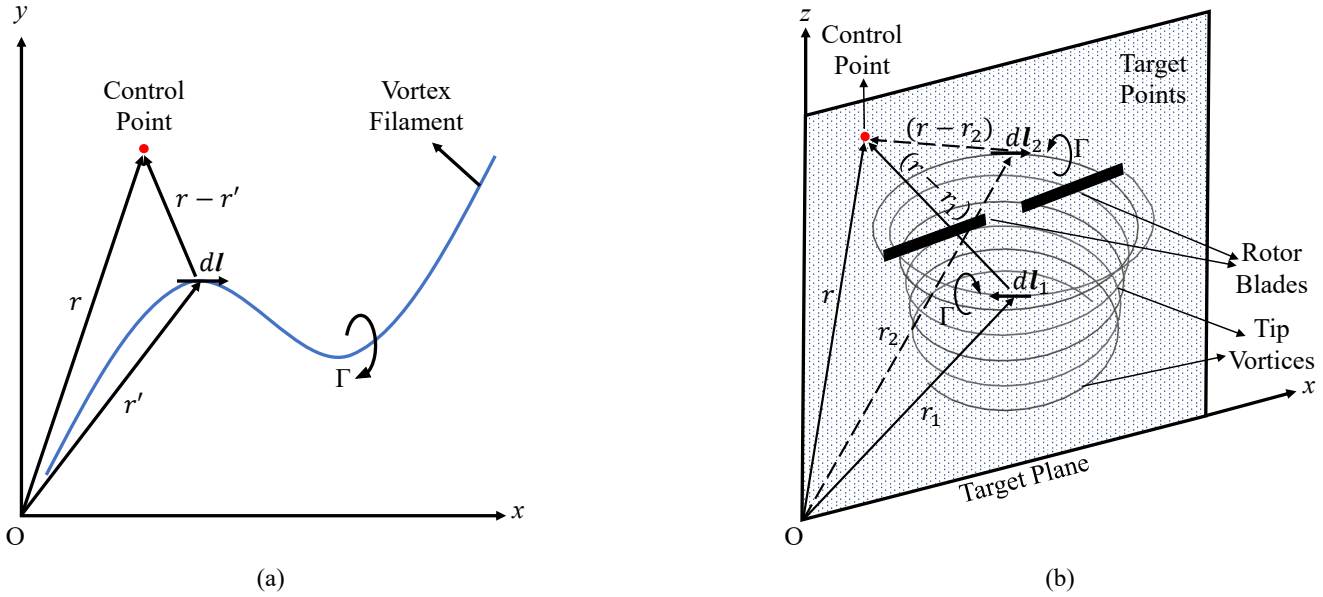

Figure 4. Induced velocity computation using the Biot–Savart law: **(a)** Induced velocity evaluation at a control point due to a vortex filament; **(b)** Induced velocity calculations on a representative target plane using discretized vortex segments.

https://doi.org/10.5194/egusphere-2026-977
Preprint. Discussion started: 19 March 2026

induced velocity is computed by accumulating the contributions of all such segments, at any given time step. This induced velocity calculation is used to identify the “quiet-zones" for wind sensor placement. A representative schematic of the rotor wake, a target plane, and the calculation of the induced velocity is shown in Fig. 4b.

2.2 Experimental Setup

An in-house experimental setup, as shown in Fig. 5, is utilized to validate the velocity predictions from the FVM model. The setup houses a single-rotor commercial APC 12×6E (12 inch diameter, UAV scale propeller (APC Propellers, 2025)), mounted horizontally (parallel to the ground) on a rotor test rig. The rotor is driven by A T-Motor AT3520 KV550 Long Shaft Brushless DC (BLDC) motor (T-Motor, 2024), powered by a 30,000 mAh battery with an output of 24–25 V.

The TriSonica Mini wind and weather sensor (referred to as the ‘sensor’) (LI-COR Environmental, 2025) is positioned along the rotor axis to measure the rotor-induced velocity at various downstream locations. The sensor is capable of recording flow speeds in the range of 0–50 $\mathrm{m\ s^{-1}}$ with an accuracy of ±2–4% and a resolution of 0.01 $\mathrm{m\ s^{-1}}$. In this work, the maximum possible data acquisition rate of the sensor, 40 Hz, is utilized. In addition to the velocity magnitude, the sensor reports wind direction through three orthogonal components (u, v, w), resolved to 1°. The components u and v cover 0°–359° with an angular accuracy of ±1°, while the component w measures deviations up to ±15° from the horizontal, with an accuracy of 0.2 $\mathrm{m\ s^{-1}}$. Before each test, the sensor was calibrated under quiescent ambient conditions to ensure reliable measurements. Furthermore, the vertical velocity component is excluded due to blockage effects caused by the sensor.

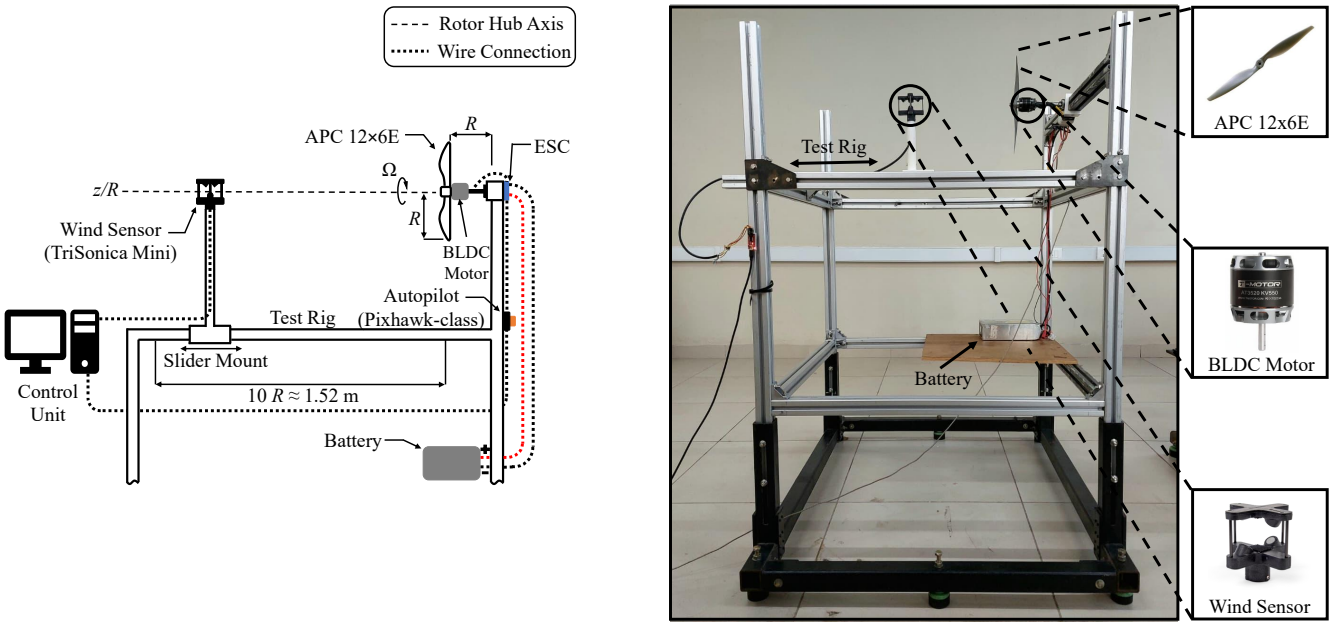

Figure 5. Schematic representation and actual image of the experimental setup and instrumentation used in the present study.

https://doi.org/10.5194/egusphere-2026-977
Preprint. Discussion started: 19 March 2026

3 Results and Discussions

The section presents the results of the present study in the following order

1. Cross-validation of the rotor-induced velocity between the in-house developed FVM solver and the experimental facility
2. Numerical studies of the flow field of the rotor in single, quad and hexa-rotor configurations of APC 12×6E (APC propeller) to identify the optimal location for the placement of the wind sensor

Prior to analyzing these results, it is critical to recognize that rotors and their operating conditions on UAVs span a wide range. Consequently, there is a need for an effective parameter that can systematically describe UAVs spanning different weight and size classes. One such parameter from the field of rotorcraft is disk loading (DL), which is defined as the ratio of the total thrust (T) generated by a rotor to the total area (A) of the rotor disk.

$$\mathrm{DL} = T/A \tag{4}$$

where $A = \pi R^2$ and R is the radius of the rotor. Disk loading is an appropriate physically meaningful and practically grounded parameter that enables generalization of the operating thrust condition of rotor systems across scales – from electrically driven small-scale UAV rotors to large-scale helicopter systems, as shown in Fig. 6. However, it is a dimensional

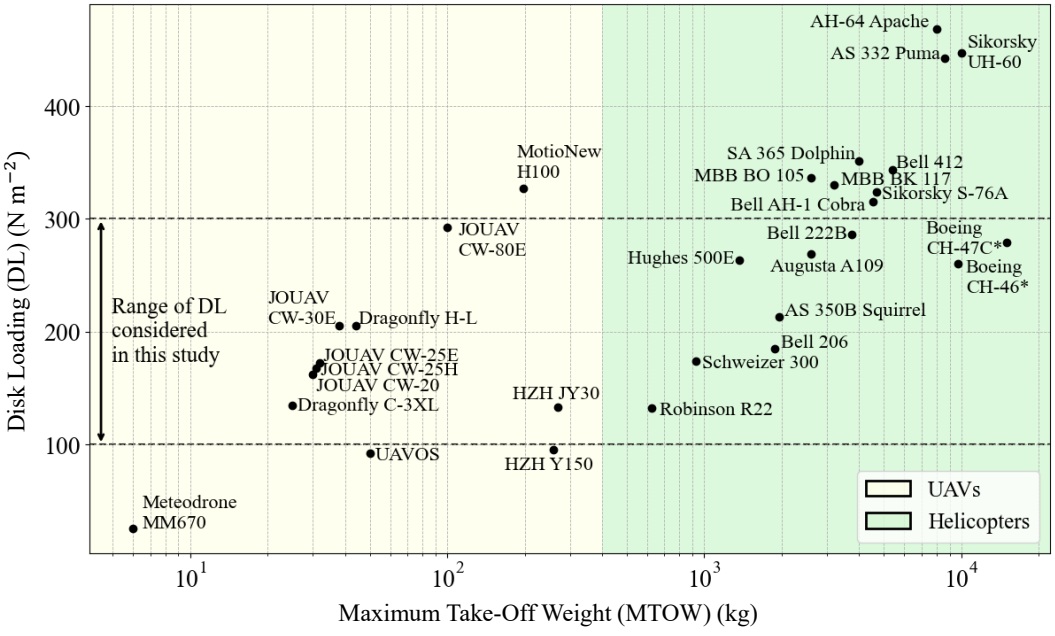

Figure 6. Maximum take-off weight (MTOW) vs. Disk loading (DL) for a range of UAVs (yellow) and helicopters (green). The typical DL range of 100–300 N m^{-2} for UAVs motivates its use in our study.

https://doi.org/10.5194/egusphere-2026-977
Preprint. Discussion started: 19 March 2026

parameter (with units of force length^{-2}), in contrast to the typically utilized non-dimensional parameters for cross-scale generalization in aerodynamics. Appendix A details the rationale behind the choice of DL for comparison. To ensure relevance and applicability of the present study to real-world systems, the distribution of disk loading was examined across a variety of commercially available UAVs and helicopter platforms. Two categories are introduced based on the Maximum Take-Off Weight (MTOW) of the rotorcraft: 1. UAVs (yellow shaded region) – These include electrically driven small-to medium scale vehicles with MTOW typically below 100 kg, and 2. Full-scale helicopters (green shaded region) – These encompass conventional combustion engine-driven vehicles with MTOWs often in excess of 1000 kg.

It is evident from Fig. 6 that most commercially available UAVs, irrespective of the vehicle's specific configuration, operate within a DL range of $\approx$ 100–300 N m^{-2} – primarily due to design constraints related to electric propulsion, battery limits, and aerodynamic efficiency. Such a trend is also visible in the helicopter regime. Consequently, for the present study, a DL range of 100–300 N m^{-2} was considered as it captures realistic operating conditions for a wide class of UAVs.

Propeller Geometry: The APC UAV-scale propeller was utilized in this study for validation and sensor placement studies. The span-wise twist and chord distributions of the APC propeller are presented in Fig. 7, and other geometry and flow parameters for the various rotor configurations considered in the study are detailed in Table. 1.

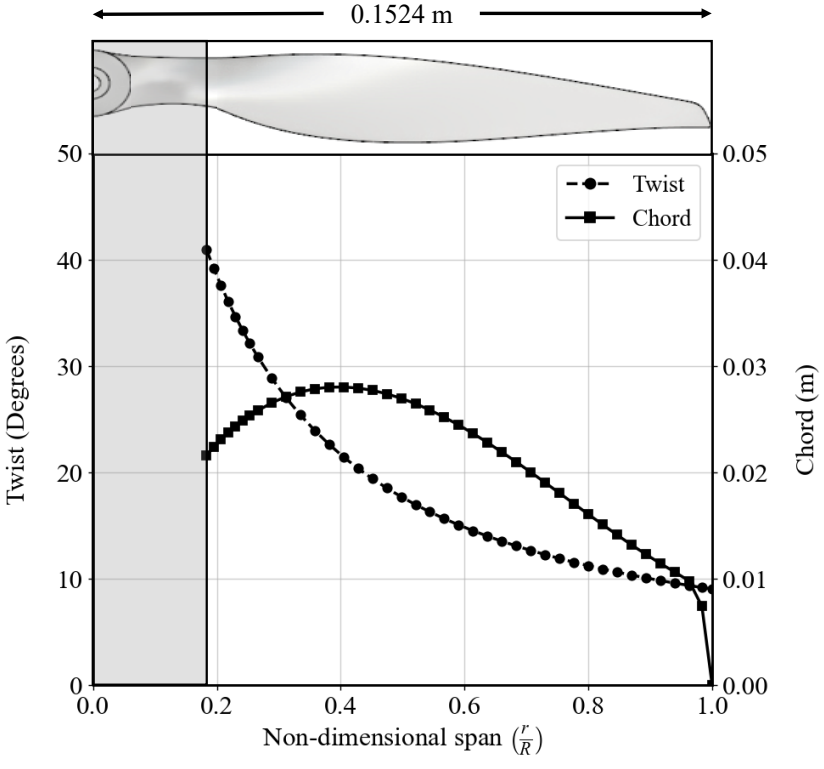

Figure 7. Span-wise twist and chord distributions of the APC propeller.

https://doi.org/10.5194/egusphere-2026-977
Preprint. Discussion started: 19 March 2026

Parameters	single-rotor	quad-rotor	hexa-rotor
Blade Radius, R (m)	0.1524	0.1524	0.1524
Root cutout, r_0 (% R)	18.33	18.33	18.33
Chord, $c(r)$ (m), and Twist, $\theta_{tw}(r)$ (°)	Refer Fig. 7	Refer Fig. 7	Refer Fig. 7
Collective Pitch, θ_0 (°)	5.6168	5.6168	5.6168
Number of blades, N_b per rotor	2	2	2
Number of rotors, N_r	1	4	6
Inter-rotor disk spacing, (% R)	...	10	10
Angular Velocity, Ω (rad s^{-1})	516–900	516–900	516–900
Tip Mach Number, M_{tip}	0.231–0.403	0.231–0.403	0.231–0.403

Table 1. Geometry and flow details of the APC single, quad, and hexa-rotor configurations.

3.1 Validation

The developed FVM model has been validated in the past work by the authors (Narayanan and Govindarajan, 2024) for the APC single-rotor thrust and power characteristics (see Appendix B, Fig. B1b and Fig. B1c). It was observed that the FVM results rendered good agreement with the manufacturer data for the propeller. To further strengthen the credibility of the developed FVM model, the rotor wake-induced velocity obtained from FVM was compared against the in-house experimental results obtained using the TriSonica wind sensor. For both the numerical and experimental analysis, the APC single-rotor was operated in hover, at a representative DL of 200 N m^{-2}, chosen as an average between the range 100–300 N m^{-2} considered for this study. The angular speed of the rotor was maintained at 748 ± 25 rad s^{-1} ($\approx 7143 \pm 239$ RPM).

Figure 8 shows the variation in the rotor-induced velocity (V_{ind}, non-dimensionalized by the rotor tip speed, V_{tip} as a function of the non-dimensional axial distance (z/R) along the rotor axis of rotation. Positive values of z/R indicate locations above the rotor plane, and negative values are locations below the rotor plane. The solid black curve corresponds to the FVM results, presented with a 1 σ standard deviation (gray-shaded band around the solid curve). The experimental data for the inflow velocity distribution across both upstream and downstream axial positions are also shown in Fig. 8, represented as black data points with a 1 σ standard deviation. The FVM predictions compare well with the experimental results above the plane of the rotor, thereby showing that the numerical model successfully captures the induced velocity distribution in this region. However, noticeable deviations appear below the rotor plane, which could be attributed to two main factors: 1. Obstructions near the rotor hub and support structures of the experimental setup (which also explains why no measurements are possible close to $z/R = 0$) and 2. The underlying potential flow formulation in FVM, which does not consider the effects of viscosity and merging, and/or breakdown of the vortices. In a dimensional context, the maximum velocity difference between the numerical (FVM) and experimental results below the rotor plane is $\approx 0.05 V_{tip}$, which for this rotor is ≈ 5 m s^{-1}, while the difference above the rotor plane is $\approx 0.005 V_{tip}$ or 0.5 m s^{-1}. For the purposes of this study where the focus is on the induced velocity calculation above the plane, this error is very much acceptable.

https://doi.org/10.5194/egusphere-2026-977
Preprint. Discussion started: 19 March 2026

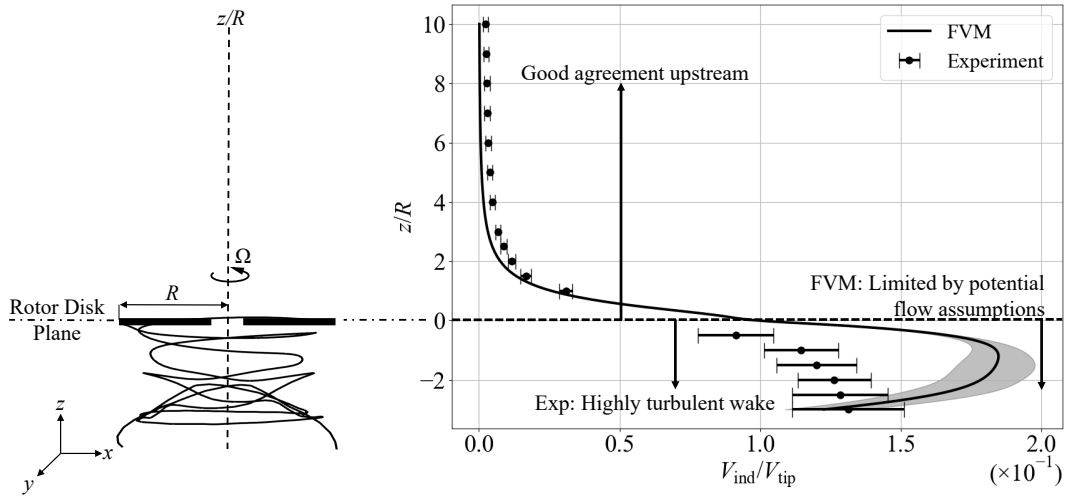

Figure 8. Comparison of induced velocity between experimental measurements and FVM predictions for the APC single-rotor. Shown on the left is the time-averaged wake representation of the rotor system from the FVM model.

3.2 Single-Rotor system

The focus of this section is on identifying quiet-zones around a simple single-rotor system in various flight conditions, which in turn will form the basis for understanding quad and hexa-rotor systems.

The APC single-rotor is considered, and the velocity induced by this rotor is calculated on an equispaced 100×100 Cartesian grid on the x–z plane at $y/R = 0$. The plane extends from $-3.5R$ to $3.5R$ along the x-axis and from $-3.0R$ to $6.0R$ along the z-axis (see Fig. 4b), where R is the radius of the rotor. The rotor's hub is located at (0,0,0), with the rotor disk in the x–y plane. All studies were performed at DL = $100\ \mathrm{N\ m^{-2}}$ and $300\ \mathrm{N\ m^{-2}}$. Results are presented over the final ten rotor revolutions, once the numerical transients in the solution and the rotor wake are allowed to settle.

In this study, three flight conditions are considered: pure hover, axial descent, and forward-flight descent. Hover represents a baseline condition and perhaps one that is most critical for collecting in situ meteorological data at a chosen altitude. In axial descent and forward descent, wake re-ingestion and strong non-uniformities of flow occur above the rotor plane, and sensor placement is very sensitive. In an axial climb scenario, the rotor wake is convected below the rotor disk, and therefore, does not induce much velocity above the plane of the rotor. Consequently, axial climb flight conditions are not presented in this paper for the sake of brevity, as they are not the limiting cases that determine the wind sensor placement location. The non-dimensional parameters defining the flight condition of the rotor are divided into the forward velocity and the axial velocity, defined as $\mu_x = V_{\text{forward}}/V_{\text{tip}}$ and $\mu_z = V_{\text{axial}}/V_{\text{tip}}$, with positive μ_z denoting axial descent, where the rotor tip speed is given by $V_{\text{tip}} = \Omega R$.

Figure 9 shows the time-averaged wake geometry overlaid on the associated velocity field for three representative flight conditions: hover, axial descent, and forward descent; shown alongside is a binary contour plot for each flight condition, which

https://doi.org/10.5194/egusphere-2026-977
Preprint. Discussion started: 19 March 2026

differentiates the flow field into two regions based on a 1% tip speed threshold for induced velocity. The binary plots indicate the "quiet-zones" in the flow field, i.e, regions where the rotor wake influences are negligible, hence defining the optimal sensor placement locations for the corresponding flight conditions. For each flight condition in Fig. 9, the left panel presents time-averaged streamlines of the total velocity field in the x–z plane. Total velocity is defined as the superposition of the wake-induced velocity and the prescribed freestream velocity ($\boldsymbol{V}_{\text{tot}} = \boldsymbol{V}_{\text{ind}} + \boldsymbol{V}_{\infty}$). The velocities ($|\boldsymbol{V}_{\text{tot}}| = V_{\text{tot}}$ and $|\boldsymbol{V}_{\text{ind}}| = V_{\text{ind}}$) are normalized by V_{tip}. The rotor blades are denoted by thick, horizontal line segments at $z/R = 0$, and the x and z axes are non-dimensionalized by the rotor radius R to ensure generality across scales. The right panel shows the binary plot, differentiated by gray-shaded regions and otherwise – dark gray denotes the regions dominated by the rotor wake, where the time-averaged induced velocity exceeds 1% of the blade-tip speed at DL = $100\ \text{N m}^{-2}$; light gray denotes the corresponding regions at DL = $300\ \text{N m}^{-2}$; and regions outside the gray-shaded region represent the quiet-zones for the corresponding DL, where the induced velocity is less than 1% of the blade-tip speed. Across all cases shown in Fig. 9, the induced velocity does not include the freestream component of the total velocity, and therefore the expectation is that the wind sensor should be placed in regions where the induced velocity goes to zero, so that only the true freestream velocity is measured.

The left panel of Fig. 9a illustrates the wake structure and flow field characteristics of the single-rotor in hover ($\mu_x = 0.00,\ \mu_z = 0.00$). The time-averaged streamlines of the total velocity field indicate that the flow above the rotor disk remains largely vertical and weakly disturbed, while strong velocity gradients are confined primarily to regions below the rotor plane. The right panel provides a more detailed analysis of this behavior, focusing on the case of DL = $300\ \text{N m}^{-2}$, as it exhibits a larger gray-shaded region (light gray) corresponding to $V_{\text{ind}}/V_{\text{tip}} > 0.01$ compared to the dark gray region at DL = $100\ \text{N m}^{-2}$. The light gray-shaded region corresponding to DL = $300\ \text{N m}^{-2}$ remains bounded to the vicinity of the rotor disk, approximately spanning $z/R \in (-3, 1.86)$ and $x/R \in (-2, 2)$. In contrast, the region outside the light and dark gray region, denoting the quiet-zone ($V_{\text{ind}}/V_{\text{tip}} \leq 0.01$) occupies a wide area above the rotor plane for $z/R \gtrsim 1.86$, suggesting that hover conditions provide a clearly defined region above the rotor plane with minimal wake influence suitable for wind sensor placement.

Figure 9b presents the corresponding results for a case of axial descent ($\mu_x = 0.00,\ \mu_z = 0.10$). The wake convects upward through the rotor disk in this regime, a feature evident in the left panel and consistent with classical vortex-ring-state behavior (Leishman et al., 2002). This upward wake displacement is also apparent with the time-averaged total velocity streamlines, where strong flow distortion both above and below the rotor plane can be observed. The right panel confirms that, for DL = $300\ \text{N m}^{-2}$, the light gray-shaded region ($V_{\text{ind}}/V_{\text{tip}} > 0.01$)) now extends symmetrically across the rotor disk, covering approximately $z/R \in (-2.5, 4.35)$ over nearly the entire lateral extent $x/R \in (-3, 3)$ of the plane considered for the calculation of the induced velocity. The dark gray region corresponding to DL = $100\ \text{N m}^{-2}$ remains confined within the light gray region. Consequently, the DL = $300\ \text{N m}^{-2}$ case can be taken as the governing scenario when defining the quiet-zone limits for sensor placement. The corresponding quiet zone, identified as the exterior region of both the light and dark gray regions, is significantly reduced and confined to regions far from the rotor disk, indicating that under axial descent conditions, most locations above the UAV are strongly influenced by the rotor wake. Consequently, axial descent offers only limited regions, located far from the vehicle, where wind sensor placement would experience minimal wake contamination.

https://doi.org/10.5194/egusphere-2026-977
Preprint. Discussion started: 19 March 2026

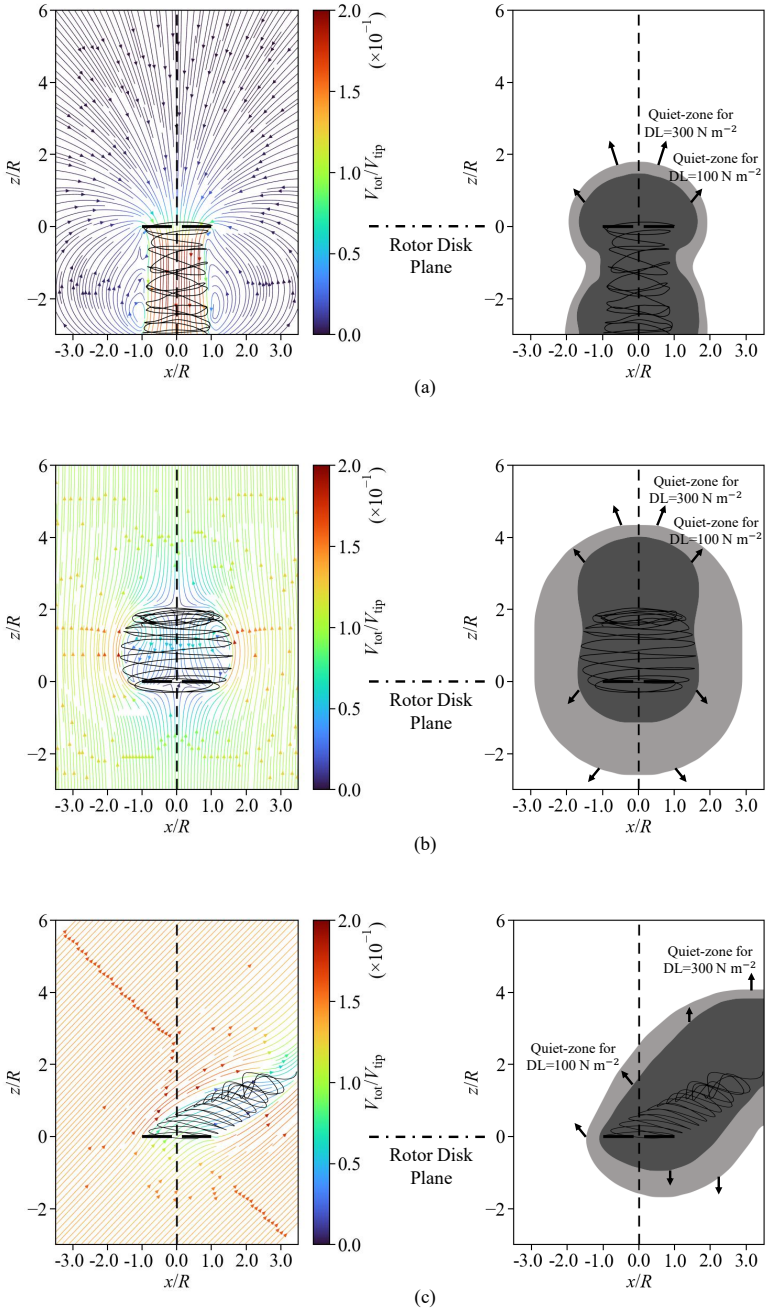

Figure 9. Flow field and wake characteristics for the APC single-rotor at DL $= 300$ N m^{-2}: **(a)** Hover ($\mu_x = 0.00,\ \mu_z = 0.00$); **(b)** Axial descent ($\mu_x = 0.00,\ \mu_z = 0.10$); **(c)** Forward descent ($\mu_x = 0.10,\ \mu_z = 0.10$). Quiet-zones are identified based on the 1% blade-tip speed threshold for induced velocity at DL $= 100$ N m^{-2} and DL $= 300$ N m^{-2}.

https://doi.org/10.5194/egusphere-2026-977
Preprint. Discussion started: 19 March 2026

For a forward descent case ($\mu_x = 0.10,\ \mu_z = 0.10$), the wake and flow field characteristics (shown in Fig. 9c along with the binary plot) reveal several interesting patterns. In this combined inflow condition (axial descent and forward flight), the left panel shows that the tip vortices are deflected downstream, forming an inclined and asymmetric wake structure. This skewing is clearly reflected by the total velocity streamlines, indicating that wake-induced disturbances are advected away from the rotor disk in the direction of flight, leading to reduced velocity gradients upstream of the vehicle. The right panel reveals a pronounced asymmetry in the distribution of wake influence: the light gray-shaded region at DL = 300 $\mathrm{N\ m^{-2}}$ is largely confined to $x/R \in (-1.8, 3.5)$. The dark gray region corresponding to DL = 100 $\mathrm{N\ m^{-2}}$ remains completely enclosed within the light gray region, indicating a comparatively reduced spatial extent of wake influence at lower disk loading. Quantitatively, a quiet-zone identified as the region outside the light and dark gray regions, with $V_{\text{ind}}/V_{\text{tip}} \leq 0.01$ is observed for $z/R \gtrsim 2.64$ at $x/R = 0$, which extends further upward than in axial descent and at lower heights (z/R) than in hover. This asymmetric quiet-region is the net effect of both forward motion and wake inclination; its location is determined by the skew angle of the wake, which is the inclination of the wake relative to the rotor axis (x). However, its suitability for wind sensor mounting has to be further investigated for different forward-descent flight regimes (different μ_x, μ_z) to reach a robust conclusion.

In general, these findings illustrate that the size and accessibility of wake-quiet regions are significantly dependent on flight conditions. In hover, a symmetric vertically separated quiet-zone exists above the rotor disk. Axial descent eliminates wake-free zones in close vicinity of the UAV, mostly above the rotor-disk, while forward flight creates an asymmetric yet accessible quiet-zone positioned upstream of the rotor, but requires detailed investigation of the wake skewness.

Further analyzing the nature of the flow field for different flight conditions, Fig. 10 presents the variation of the time-averaged induced velocity (V_{ind}) along the rotor-z-axis for three radial (blade span-wise) locations ($r/R = 0, \pm 1$, presented in blue, red, and green colors, respectively, as shown in Fig. 10a). The induced velocity is normalized by V_{tip}, while the rotor axis is normalized by the rotor Radius (R). The shaded bands represent the standard deviation of the induced velocity, corresponding to a 1 σ variation about the mean, evaluated over the final ten rotor revolutions of the converged solution, indicating the temporal variability of the induced flow.

For hover (Fig. 10b), at the rotor hub plane ($r/R = 0$), the time-averaged induced velocity values are negligible upstream of the rotor disk ($z/R > 1.86$). A pronounced peak can however be observed immediately downstream ($z/R \approx -1$) of the rotor disk plane, associated with wake contraction; the peak gradually decays farther downstream as the wake expands and diffuses, indicating that the region below the rotor ($z/R < -1$) is unsuitable for wind-speed measurements. A similar aerodynamically dirty downstream region can be observed for the other radial locations ($r/R = \pm 1$), owing to tip-vortex shedding, and strong wake interactions. The induced velocity values upstream of the rotor disk still remain negligible for practical purposes. In axial descent (Fig. 10c), elevated induced velocities persist both above and below the rotor disk plane over a wide axial extent ($z/R \in (-2.50, 4.35)$, reflecting the upward convection of the wake through the disk; although an apparent decay is observed for $z/R \gtrsim 4.35$, this behavior is partly attributable to truncation of the helical wake in the numerical solution, and in practice all regions above the rotor remain affected by rotor-induced flow. In forward-descent flight (Fig. 10d), the upstream induced velocity distribution becomes strongly dependent on radial position and direction, with quieter regions occurring at substantially lower heights above the rotor plane on the retreating side ($r/R = -1$) than on the advancing side ($r/R = +1$),

https://doi.org/10.5194/egusphere-2026-977
Preprint. Discussion started: 19 March 2026

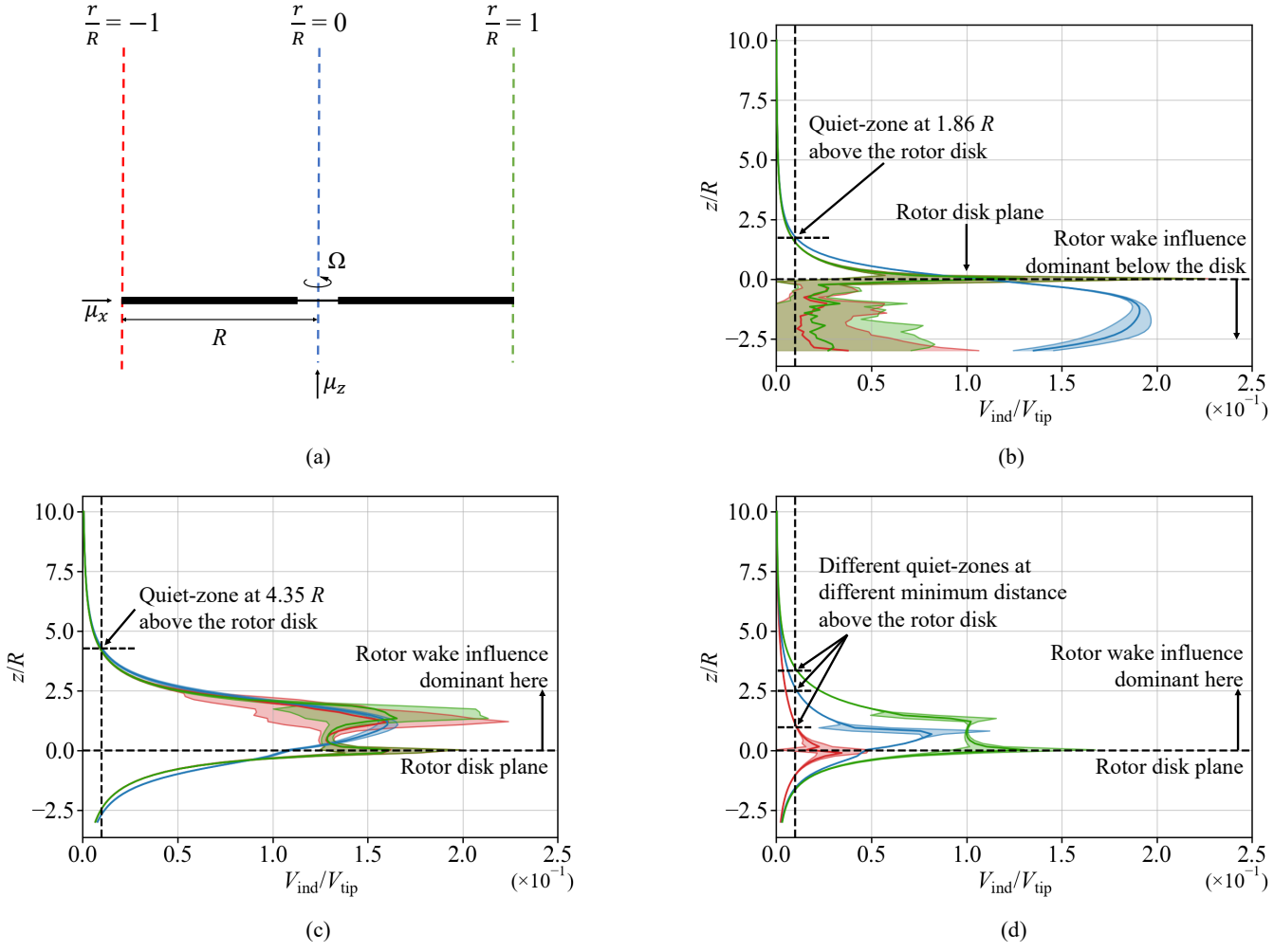

Figure 10. Axial variation of induced velocity for the APC single-rotor at various span-wise locations: **(a)** Span-wise locations considered for induced velocity analysis; **(b)** Hover ($\mu_x = 0.00,\ \mu_z = 0.00$); **(c)** Axial descent ($\mu_x = 0.00,\ \mu_z = 0.10$); **(d)** Forward descent ($\mu_x = 0.10,\ \mu_z = 0.10$), all at DL = 300 N m^{-2}.

as a consequence of the skewed wake geometry. Overall, these results demonstrate that potential sensor placement regions are highly dependent on flight condition, with viable low-disturbance zones emerging only when wake inclination (wake skew angle) displaces rotor-induced flow away from the measurement location.

To attain a comprehensive understanding of the influence of the flight condition on the quiet-zones for wind-sensor placement, various combinations of axial and forward speeds are studied in detail. Figure 11 presents the minimum axial distance of the quiet-zone from the rotor disk, normalized by the rotor radius ($(z/R)_{\text{min}}$), as shown in Fig. 11a for four different descent conditions ($\mu_z = 0.05,\ 0.10,\ 0.15,\ 0.20$). The quiet-zone is delineated from the binary plot for each case (similar to the right panel of Fig. 9). For each of the descent case, the minimum quiet-zone distance $(z/R)_{\text{min}}$ was obtained for various forward

https://doi.org/10.5194/egusphere-2026-977
Preprint. Discussion started: 19 March 2026

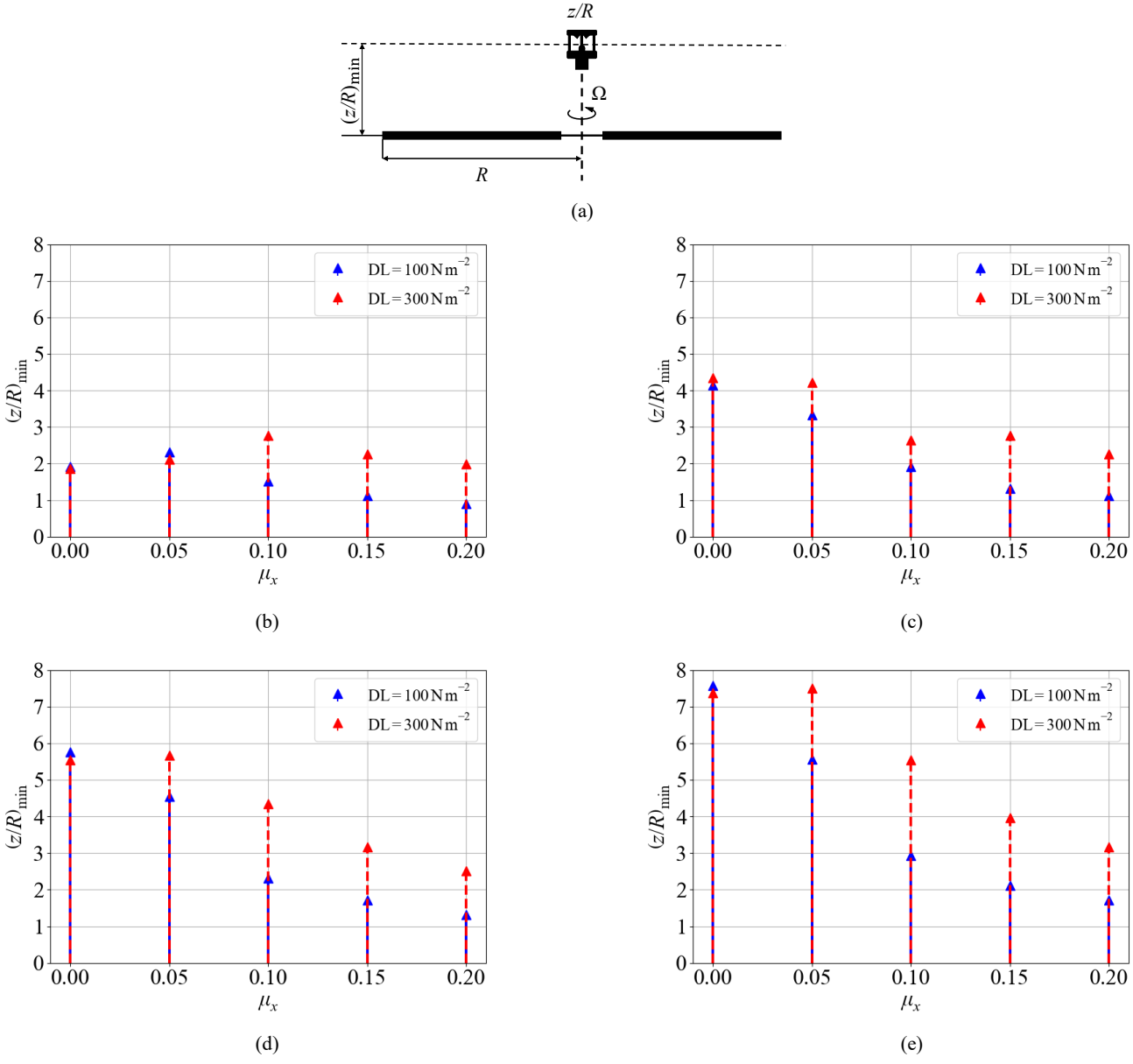

Figure 11. Variation of the minimum axial location of the quiet-zone at the rotor hub for the APC single-rotor: **(a)** Schematic representation of the definition of $(z/R)_{\text{min}}$; **(b)** $\mu_z = 0.05$; **(c)** $\mu_z = 0.10$; **(d)** $\mu_z = 0.15$; **(e)** $\mu_z = 0.20$.

flight speeds (given by advance ratio $\mu_x = 0.00,\ 0.05,\ 0.10\ 0.15\ 0.20$, where $\mu_x = 0.0$ is pure descent, and the other cases correspond to various forward-descent conditions). Two DL values are presented in each case, chosen as the typically observed lower and upper limits for UAVs. Additionally, a schematic showing the minimal axial distance on the single-rotor is also presented; in the interest of brevity, only the hub plane $(r/R = 0)$ results are presented here.

https://doi.org/10.5194/egusphere-2026-977
Preprint. Discussion started: 19 March 2026

For the weak axial descent case $\mu_z = 0.05$ (Fig. 11b), $(z/R)_{\text{min}}$ initially increases with μ_x, reaching a maximum around $\mu_x = 0.05,\ 0.10$ for the low and high DL cases, respectively, before decreasing as μ_x increases further (This non-monotonic behavior arises from a transition between a predominantly axisymmetric wake at low μ_x and a progressively skewed wake at higher μ_x, where downstream convection brings the low-disturbance region closer to the rotor plane). In the moderate axial descent case $\mu_z = 0.10$ (Fig. 11c), $(z/R)_{\text{min}}$ decreases with increasing μ_x for the lower DL case. The higher DL case demonstrates the decrease in $(z/R)_{\text{min}}$ up to $\mu_x \approx 0.10$, followed by a brief increase peaking around $\mu_x = 0.15$, before decreasing again at higher μ_x (This behavior reflects competing effects between wake skewing, which generally lowers $(z/R)_{\text{min}}$, and localized wake thickening caused by the interaction of axial inflow with edgewise motion).

For stronger axial descent conditions $\mu_z = 0.15$ and $\mu_z = 0.20$ (Figs. 11d and 11e), $(z/R)_{\text{min}}$ decreases more consistently with increasing μ_x. a trend that is most clearly observed for the higher disk loading case DL = 300 N m^{-2} (under strong axial inflow, the wake remains more coherent and aligned with the rotor axis, and increasing edgewise motion primarily skews the wake away from the rotor-hub axis, reducing the axial extent of the disturbed region). In contrast, except for the $\mu_z = 0.05$ case, the lower disk loading condition (DL $= 100$ N m^{-2}) exhibits a consistently monotonic decrease of $(z/R)_{\text{min}}$ with μ_x for a given μ_z (weaker induced velocities result in a more rapidly convected wake, limiting upstream disturbance).

Across both DL cases, $(z/R)_{\text{min}}$ generally increases with increasing magnitude of axial descent μ_z for a fixed μ_x (because stronger axial inflow intensifies the induced velocity field and displaces the disturbed wake region farther upstream). Notably, for pure axial descent conditions with $\mu_x = 0.0$, the values of $(z/R)_{\text{min}}$ for DL $= 100$ N m^{-2} and 300 N m^{-2} are nearly identical (since in the absence of edgewise motion, wake symmetry dominates and DL primarily scales velocity magnitude rather than wake topology). The hover condition ($\mu_x = 0.0,\ \mu_z = 0.0$) is not included, as the present analysis emphasizes on non-hover flight regimes, where wake asymmetry and axial inflow effects significantly influence sensor placement. Overall, these results indicate that optimal wind-speed sensor placement requires the greatest axial separation under weak axial descent, while forward-descent conditions permit sensor placement closer to the rotor plane, with higher DL consistently increasing the required clearance.

3.3 Multi-Rotor Systems

The single-rotor analysis is extended to quad-rotor and hexa-rotor configurations, to ensure applicability to practical configurations in the UAV space, where such multi-rotor systems are the predominant design choice. The APC propeller (refer Table. 1 for the geometry data) is considered for both the multi-rotor configurations, and the time-averaged total velocity streamlines, along with the quiet-zone binary plots are presented at two different x–z planes passing through different regions of the rotor system. Only the hovering flight condition is discussed in this section for the following reasons

1. One of the primary meterological applications is that of wind speed measurements, and VTOL multi-rotor systems allows for point measurements in space over a long time-period. Consequently, hover is the most critical flight condition.

2. Similar to the results seen with the single rotor system, a descending flight condition will cause the rotor wake to be convected up through the rotor disk, and will interfere with the sensor signals. A similar argument can be made for

https://doi.org/10.5194/egusphere-2026-977
Preprint. Discussion started: 19 March 2026

descending forward flight conditions as well. Therefore, in the interest of brevity, only hovering flight is presented with a focus on wind sensor placement locations.

3.3.1 Quad-rotor

Figure 12a shows the configuration of the APC quad-rotor system considered in the study. The rotor disk is positioned along the x–y plane with inter-rotor spacings chosen appropriately based on existing UAVs. For the induced velocity computations, two equispaced 100×100 Cartesian grids in the x–z plane are chosen; (a) Plane I, passing through the geometric center of the system (GC) at (0,0,0), and (b) Plane II, passing through the hubs of rotors 1 $(-1.05R,\ 1.05R,\ 0)$ and 4 $(1.05R,\ 1.05R,\ 0)$, respectively, as shown in Fig. 12b. The wake from each rotor is split into blue and red color, to highlight the blade from which these vortices are trailed. Compared to a single-rotor wake, the structure beneath the quad-rotor is a bit more complex owing to significant rotor-rotor interactions. The target planes extend from $-3.5R$ to $3.5R$ along the x-axis and from $-3.0R$ to $6.0R$ along the z-axis. All investigations are conducted on a DL of 100 N m^{-2} and 300 N m^{-2}, and similarly to the case of the single-rotor, results are reported over the final ten revolutions of the rotor, after the numerical transients in the solution are allowed to settle.

Figure 13 illustrates the flow field characteristics of the quad-rotor system in hover, on the two planes shown in Fig. 12. The panels on the left present the total velocity streamlines normalized by V_{tip}, while the right panels represent the quiet-zones

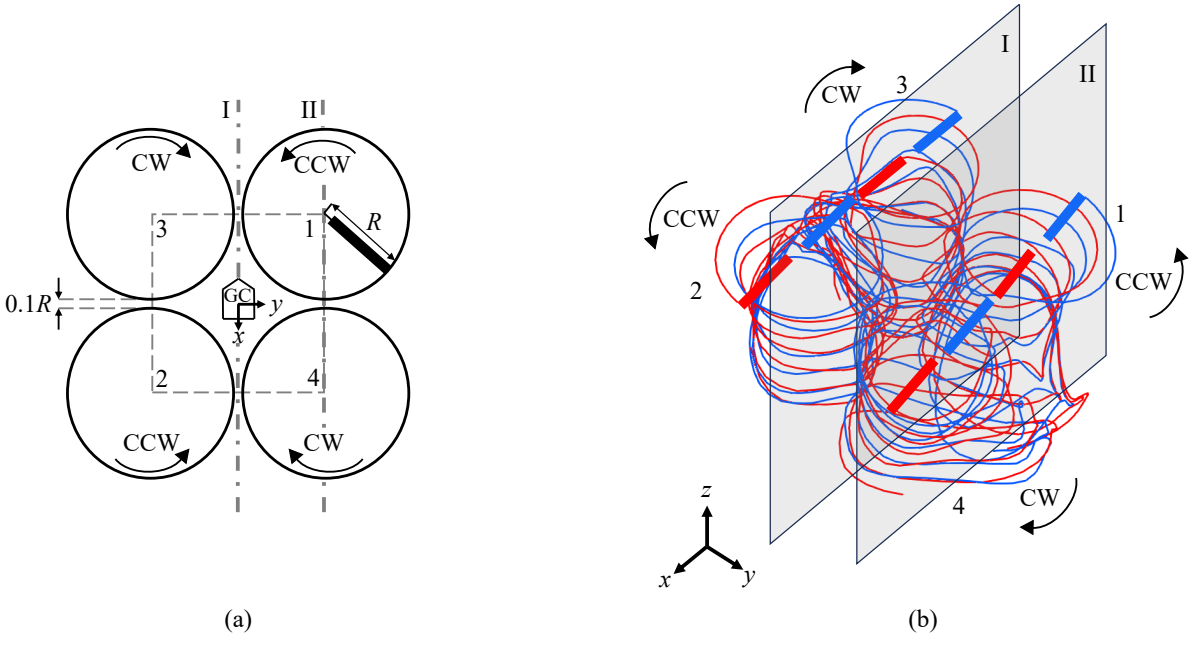

Figure 12. Quad-rotor configuration and corresponding time-averaged wake trajectories: **(a)** Quad-rotor configuration utilized in the present study; **(b)** Isometric view of the calculated time-averaged wake trajectories of all rotors in the quad-rotor configuration.

https://doi.org/10.5194/egusphere-2026-977
Preprint. Discussion started: 19 March 2026

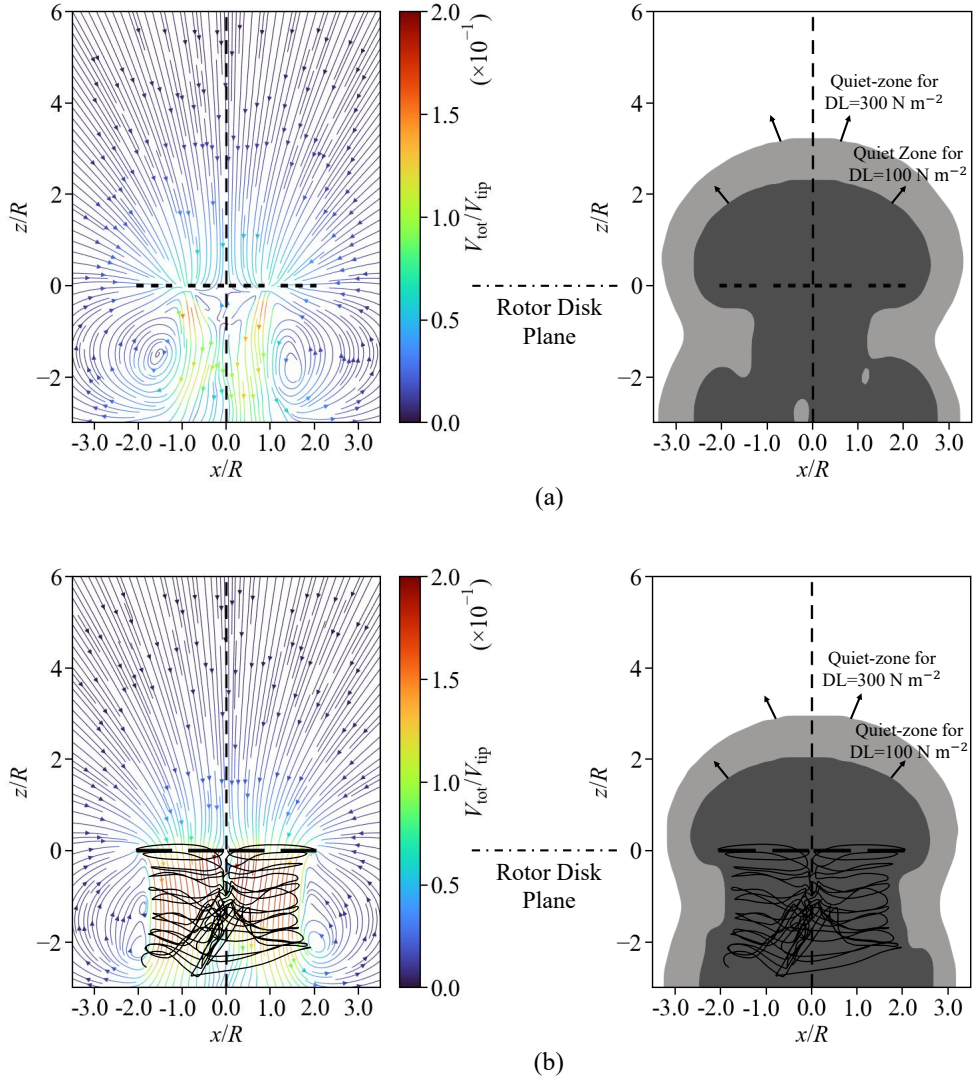

Figure 13. Flow field and wake characteristics for the APC quad-rotor in hover at DL $= 300$ N m^{-2}: **(a)** x–z plane passing through the geometric center (Plane I); **(b)** x–z plane passing through the hubs of rotors 1 and 4 (Plane II). Quiet-zones are identified for DL $= 100$ N m^{-2} and DL $= 300$ N m^{-2}.

identified using the 1% blade-tip speed threshold for the induced velocity. The dark gray regions correspond to the locations where the magnitude of the induced velocity satisfies $(V_{\text{ind}}/V_{\text{tip}} > 0.01)$ at DL = 100 N m^{-2}, while the light gray regions denote the corresponding locations at DL = 300 N m^{-2}. Consequently, regions outside the dark gray zone are quiet-zones for

https://doi.org/10.5194/egusphere-2026-977
Preprint. Discussion started: 19 March 2026

DL = 100 N m^{-2}, and those outside the light gray are quiet-zones at the higher disk loading. As expected, if the DL is higher, then the sensor has to be placed further away from the rotor disk plane compared to if the DL is lower.

Figure 13a shows the time-averaged streamlines and the threshold plot for Plane I. The horizontal dashed line segments at $z/R = 0$ indicate the projected blade locations in the y-direction, since the rotor disks are not visible in this plane. The flow field below the rotor disk plane is governed by the interaction of the individual rotor wakes, an inherently unsteady process. Although instantaneous structures are highly transient, the time-averaged streamlines on the left panel (Fig. 13a) indicate a complex but organized wake topology, with symmetric recirculation regions formed by the merging rotor-induced vortices. The light gray region (right panel), corresponding to DL = 300 N m^{-2}, extends further above the rotor disk plane than the dark gray region at DL = 100 N m^{-2}, while the extent below the disk remains comparable for both cases. This indicates that increased disk loading primarily enlarges the wake-dominated region above the rotor plane defined by $V_{\text{ind}}/V_{\text{tip}} > 0.01$. The minimum axial location above the disk plane at the GC that satisfies the induced velocity threshold is $(z/R)_{\text{min}} \approx 3.30$ at the higher disk loading and ≈ 2.10 at the lower disk loading.

Figure 13b presents the corresponding flow field for Plane II, where the plane intersects the rotor disks of rotors 1 and 4. At the GC, the induced velocity field above the rotor plane is stronger, which may be attributed to the cumulative superposition of the induced velocity components from all four rotors, leading to a locally amplified upward influence in the central region. The regions defined by the 1% blade-tip speed threshold further highlight this distinction. Consequently, the quiet-zone defined by $V_{\text{ind}}/V_{\text{tip}} \leq 0.01$ is achieved at a slightly lower axial location for Plane II, with $(z/R)_{\text{min}} \approx 3.17$, compared to $(z/R)_{\text{min}} \approx 3.30$ at the GC, for a similar lateral extent of $x/R \in (-3.5, 3.5)$. Assuming geometric symmetry in hover, a plane passing through the hubs of rotors 2 and 3 may be expected to exhibit behavior similar to Plane II. Therefore, under hover and axial climb conditions, where wake development is predominantly directed below the rotor disks, a plane such as Plane II offers a comparatively more favorable location for wind sensor placement than the GC, owing to the earlier attainment of the quiet-zone above the rotor plane.

It is noted, however, that the difference in axial extent between the two configurations is relatively small, with $\Delta(z/R) = 0.13$. Therefore, if structural or airframe constraints limit sensor placement to the GC, it may still be considered a viable mounting location, as the increase in the minimum threshold height remains modest.

3.3.2 Hexa-rotor

A hexa-rotor configuration of the APC rotor is shown in Fig. 14a. The rotor disk is positioned along the x–y plane. For the induced velocity computations, three equispaced 100 × 100 Cartesian grid in the x–z, and y–z planes are chosen – Plane I, passing through the system GC at (0,0,0), Plane II, passing through the hubs of rotor 3 $(1.82R,\ -1.05R,\ 0)$ and 5 $(1.82R,\ 1.05R,\ 0)$, and Plane III, passing through the hubs of rotor 4 $(-1.82R,\ 1.05R,\ 0)$ and 5 $(1.82R,\ 1.05R,\ 0)$. The target planes extend $-3.5R$ to $3.5R$ along the x and y-axis, and from $-3.0R$ to $6.0R$ along the z-axis. All investigations are performed at a DL of 100 N m^{-2} and 300 N m^{-2}, and results are presented over the final ten rotor revolutions of the simulation, after transients in the solution are allowed to settle. Results presented are similar to the quad-rotor system – the time-averaged streamlines and the quiet-zone plot, for three planes (Planes I, II, and III) shown in Fig. 14.

https://doi.org/10.5194/egusphere-2026-977
Preprint. Discussion started: 19 March 2026

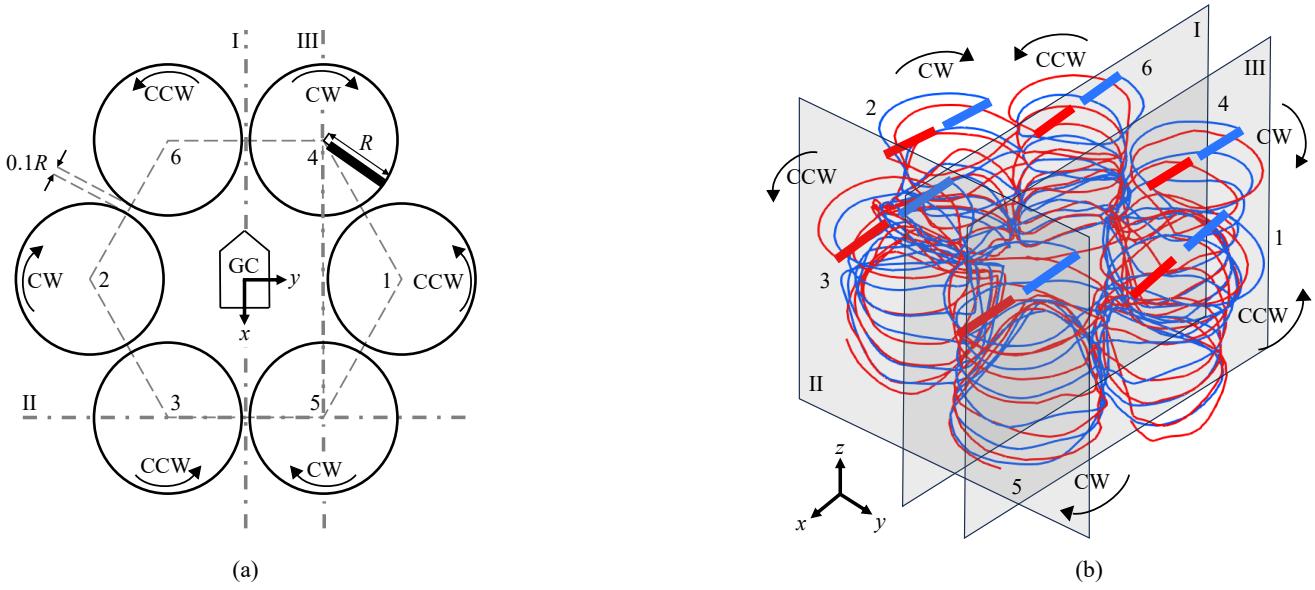

Figure 14. Hexa-rotor configuration and corresponding time-averaged wake trajectories: **(a)** Hexa-rotor configuration utilized in the present study; **(b)** Isometric view of the calculated time-averaged wake trajectories of all rotors in the configuration.

The flow field characteristics of the hexa-rotor in hover, are shown in Figure 15 for the three planes, I–III. Similar to the quad-rotor results, the panels on the left of Fig. 15 depict the time-averaged total velocity stream-lines, and the right panels illustrate the binary plots for quiet-zone detection, based on the 1% tip speed threshold for the induced velocity. The dark gray regions in the right panels indicate areas where the time-averaged induced velocity exceeds the specified threshold for DL = $100\ \mathrm{N\ m^{-2}}$, whereas the light gray regions denote the corresponding regions for DL = $300\ \mathrm{N\ m^{-2}}$.

At Plane I (refer to Fig. 14), the time-averaged streamlines on the left panel reveal a considerably aysmmetric flow field beneath the rotor system. In practice, these wake structures are considerably aperiodic, which may be the reason for the lack of a symmetric structure even in the time-averaged sense. Since none of the rotor disks intersects this plane, the horizontal dashed line segments at $z/R = 0$ denote the projection of the rotor blades in the y-direction, representing the plane of the rotor disk. Higher magnitudes of the induced velocity extend laterally beyond the projected rotor disks along x/R, indicating pronounced cross-rotor wake interactions near the system GC. The binary plot in the right panel of Fig. 15a identifies regions where the time-averaged induced velocity exceeds the 1% blade-tip speed threshold. In the vicinity of the GC and within $x/R \in (-1.0, 1.0)$, the total velocity below the rotor disk is directed upward and briefly crosses the rotor plane, persisting up to approximately $z/R \approx 0.27$. Immediately above this location, for $z/R \gtrsim 0.27$, the velocity reverses direction and becomes downward, consistent with the normal inflow direction above a hovering rotor. The opposing contributions near this axial location result in a local reduction of the magnitude of the induced velocity, leading to a narrow quiet-zone window for both DL = $100\ \mathrm{N\ m^{-2}}$ and DL = $300\ \mathrm{N\ m^{-2}}$. However, this cancelation is confined to a limited axial extent. Beyond this brief

https://doi.org/10.5194/egusphere-2026-977
Preprint. Discussion started: 19 March 2026

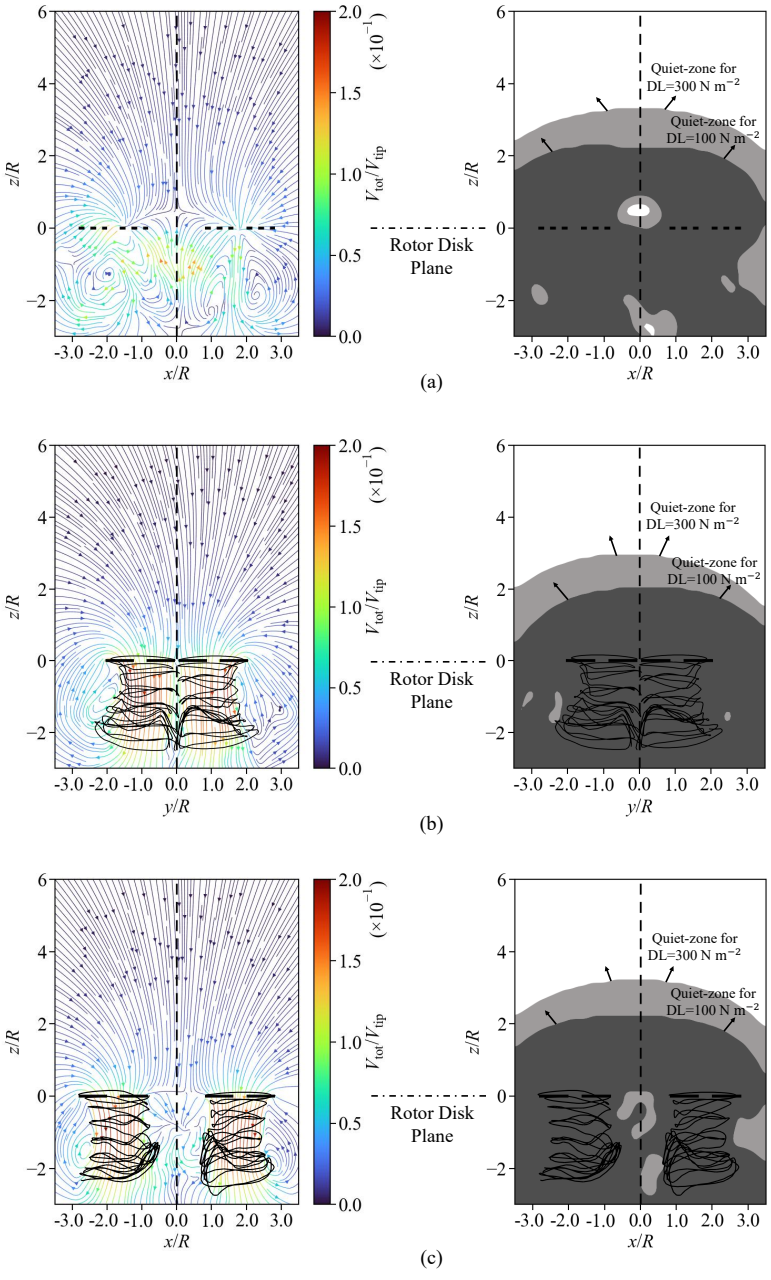

Figure 15. Flow field and wake characteristics for the APC hexa-rotor in hover: **(a)** x–z plane passing through the geometric center (Plane I); **(b)** y–z plane passing through the hubs of rotors 3 and 5 (Plane II); **(c)** x–z plane passing through the hubs of rotors 4 and 5 (Plane III). Results shown at DL $= 300$ N m^{-2} with corresponding quiet-zone identification for DL $= 100$ and 300 N m^{-2}.

https://doi.org/10.5194/egusphere-2026-977
Preprint. Discussion started: 19 March 2026

window, the cumulative induced field from the six rotors dominates, leading to $V_{\text{ind}}/V_{\text{tip}} > 0.01$ above the disk plane. The wake-dominated region extends further upstream for DL = 300 N m^{-2} than for DL = 100 N m^{-2}, reflecting the stronger global induced field associated with higher disk loading. The minimum axial location at which the threshold is satisfied at the GC is $(z/R)_{\text{min}} \approx 3.36$, beyond which a sustained quiet-zone is established.

Figures 15b and 15c depict the flow field characteristics on planes II and III, respectively. Both planes pass through two rotors each – Plane II, passing through adjacent rotors (3, and 5) separated by $0.1R$ between the rotor tips, and Plane III, passing through rotors (4, and 5), the distance between the tips of the rotors being $\approx 3.6R$. A qualitative analysis of the wake behavior for both planes II and III reveal that the proximity of the rotors to each other and the surrounding rotors create strong rotor-wake interactions downstream of the rotor system, which in turn affect the induced velocity distribution. Such interactions are predominant around $z/R \approx -2$, as can be observed from the left panels of Figures 15b and 15c present the time-averaged stream-lines for planes passing through rotors 3–5 and 4–5, respectively. The wake interaction below the disks remains strong in both planes, while a localized reduction in the magnitude of the induced velocity is observed along the plane centerline $(x/R = 0)$ in Plane III (Fig. 15c). This reduction is primarily influenced by the nearby counter-rotating rotor 1, whose opposing azimuthal velocity component partially offsets the swirl induced by rotors 4 and 5 in the inter-rotor region, thereby decreasing the net induced velocity magnitude along the centerline. The binary plots (right panels) provide a clearer assessment of the quiet-zone extent. For the plane intersecting rotors 3 and 5 (Fig. 15b), the induced velocity threshold is satisfied at $(z/R)_{\text{min}} \approx 3.17$ for DL = 300 N m^{-2}. For the plane intersecting rotors 4 and 5 (Fig. 15c), the corresponding value is slightly higher, at $(z/R)_{\text{min}} \approx 3.27$ at the same DL. Although a localized reduction in the induced velocity is evident along the centerline in Plane III, a similar feature is not prominently observed in Plane II. However, in both cases, the flow immediately upstream of the individual rotor disks continues to exhibit $V_{\text{ind}}/V_{\text{tip}} > 0.01$, which limits the practical placement of a wind-speed sensor near the rotor disk. Comparing these results with the GC configuration, where $(z/R)_{\text{min}} \approx 3.36$, the planes may be ranked in increasing order of minimum quiet-zone height as: Plane II, Plane III, and Plane I (GC). Thus, from a purely aerodynamic standpoint, the plane passing through rotors 3 and 5 (Plane II) offers the most favorable axial location for sensor placement, as it achieves the quiet-zone at the lowest normalized height. Nevertheless, practical integration constraints must also be considered. The structural layout or components of the airframe may restrict asymmetric placement, and this result captures only the solution of hovering. The placement at GC may be preferable when all flight conditions are to be considered. In particular, for sensors of compact dimensions, installation near the localized quiet-zone window may still be feasible without significant degradation in measurement fidelity. Therefore, careful coordination between aerodynamic, structural, and flight stability considerations is required to determine the final mounting location.

4 Summary and Conclusions

Current atmosphere measurement techniques utilize single-use systems or expensive ground-based instruments, among several other methods. The potential for instrumented vertical takeoff and landing Unmanned Aerial Vehicles (VTOL-UAVs) to complement (and in some cases replace) existing techniques is immense, given the higher accessibility, controllability, and res-

https://doi.org/10.5194/egusphere-2026-977
Preprint. Discussion started: 19 March 2026

olution of the measurements possible with these systems. A critical decision is the placement of wind-speed and other sensors that are sensitive to surrounding flow. To that end, the present study examines the influence of rotor-induced flow on single and multi-rotor systems, with the objective of identifying quantitatively reliable locations, or "quiet-zones", devoid of wake effects that are suitable for positioning wind-speed measurement (or other) sensors. An in-house, free-vortex wake model (FVM) framework is utilized, and the flow field characteristics of isolated UAV-scale single, quad, and hexa-rotor systems are studied under various flight conditions of hover, axial descent, and forward descent. The rotor systems are operated at a disk loading (DL) of $100\ \mathrm{N\ m^{-2}}$ and $300\ \mathrm{N\ m^{-2}}$ to ensure a physically meaningful comparison that is independent of the vehicle scale or configuration. Validation of the FVM model is carried out against in-house experimental velocity measurements, to strengthen the credibility of the FVM model in capturing key flow field features. A 1% tip speed threshold (translates to roughly less than $1\ \mathrm{m\ s^{-1}}$ for most designs) is defined for the induced velocity, to identify quiet-zones in a flow field, which subsequently translates into the optimal regions for wind-sensor placement.

Specific conclusions from the present study are as follows.

1. **Single-rotor**: It was observed that the extent of the quiet-zones was governed by the flight condition of the vehicle, with hovering flight being the practical limiting condition.

   (a) In hover, the wake is confined to downstream of the rotor disk plane, resulting in symmetric, and well-defined quiet-zones above and to the side of the rotor disk. Immediately above the rotor, the sensor can be placed at a minimum distance of $\approx 1.75R$ based on the defined threshold. As expected, sensor placement below the rotor disk would result in significant flow from the rotor wake. Sensors can also be placed laterally along the plane of the rotor from a minimum distance of $2R$, if required.

   (b) In axial descent, there exists no optimal sensor placement location upstream or downstream of the rotor disk owing to the complex wake topology surrounding the rotor system across a wide lateral extent. In a practical scenario, there would be no viable location below the rotor due to the presence of a fuselage (out of the scope of this study).

   (c) In forward descent, based on the specific flight trajectory, there exist limited quiet-zones above the rotor disk as the wake is convected away from the disk owing to the freestream velocity at a skew angle. Sensor placement can be considered on the basis of specific mission requirements.

2. **Multi-rotor systems**: Flow around the quad-rotor and hexa-rotor configurations are considerably complex owing to rotor-rotor interactions, which results in a wide spatial region around the rotor system where the induced flow is significant. Consequently, quiet-zones for sensor placement are $\approx 1.75R$–$3R$ (lower and higher DL of $100\ \mathrm{N\ m^{-2}}$ and $300\ \mathrm{N\ m^{-2}}$, respectively) away from the disk plane, at the vehicle geometric center for the two multi-rotor configurations.

3. By focusing on the primary flow field characteristics of various rotor systems, the present study offers quantitative and qualitative guidance for the placement of sensor for atmospheric measurements on VTOL multi-rotor systems. The practical choice of sensor location will also be driven by constraints in airframe design and flight stability considerations.

https://doi.org/10.5194/egusphere-2026-977
Preprint. Discussion started: 19 March 2026

Appendix A: Disk loading as a suitable parameter for rotorcraft across various weight scales

The underlying geometric parameters of rotor systems (from UAVs to helicopters) vary significantly with the application and the associated requirements. Therefore, it is imperative to generalize the results of the present work across rotor systems of different scale to ensure relevance across such applications. Generalization demands similarity in the operating conditions of the rotor systems and an underlying independent parameter that can effectively represent this similarity.

The literature on rotorcraft usually employs the blade loading coefficient (C_T/σ) to compare the aerodynamic performance of various rotor systems. Here, C_T is the thrust coefficient (non-dimensional thrust) and σ is the rotor solidity (effective blade area in a rotor with respect to its disk area). In large-scale combustion-powered helicopters, the thrust is varied through collective pitch control θ_0, while Ω is kept constant, rendering C_T/σ an effective parameter for comparison. The operational characteristics of small-scale electric UAVs are fundamentally different, wherein, thrust is modulated primarily by changes in the rotational (or angular) speed Ω of the motor and not the collective pitch θ_0. Since the thrust coefficient C_T is a function of Ω $\left(\text{ i.e., } C_T \propto T/(\rho\Omega^2 R^4)\right)$, any variation in Ω leads to a corresponding variation in C_T, thus lending C_T/σ an inconsistent parameter for comparing electrically driven variable RPM rotor performance. Therefore, the present work utilizes disk loading (DL) to compare rotor systems of various scales. DL is also defined in the literature on the rotorcraft as the ratio of the thrust generated by the rotor to its disk area $\text{DL} = T/A$.

DL is directly tied to the generated thrust and does not depend on Ω. As such, DL provides a more robust and physically meaningful basis for comparing rotors across different sizes and control mechanisms in hover. Despite being a dimensional quantity, DL is better suited for capturing the key aerodynamic similarities in our context, thereby justifying its use in the comparative analysis presented in this study. An example of the similarity in the rotor induced inflow across rotor systems of different scales operating at the same DL is given in Fig. A1.

Three different rotor systems are considered for the flow similarity analysis, as listed below

1. **HSR (Harrington single-rotor)** (Harrington, 1951): A full-scale helicopter rotor with a radius of $R = 3.81$ m
2. **APC** (APC Propellers, 2025): A commercial small-scale UAV propeller from APC with a radius of $R = 0.15$ m
3. **HW** (HobbywingDirect, 2025): A commercial medium-scale UAV propeller from Hobbywing with a radius of $R = 0.31$ m

The rotors are operated in hover, at DL = 100 N m^{-2}, by calculating the rotational speed (Ω) and the rotor collective pitch (θ_0). The time-averaged rotor-induced velocity along the normalized rotor axis (z/R) is obtained at the rotor hub plane $(r/R = 0)$ for all the three propellers, as shown in Fig. A1. The HSR is shown in red, the APC rotor in blue and the HW rotor in green, with a 1 σ standard deviation shaded band, representative of the instantaneous fluctuations in the induced velocity.In addition, the induced velocity is non-dimensionalized by the rotor tip speed (V_{tip}) to facilitate comparison across the rotor systems. It can be observed that all the three rotors exhibit similar trends in the non-dimensional induced velocity distribution, and are bounded by similar limits in both axes, revealing the similarity in the flow and wake characteristics encountered by the rotor systems. Despite vast differences in physical scale and rotor geometry, Fig. A1 reveals that the induced velocity curves

https://doi.org/10.5194/egusphere-2026-977
Preprint. Discussion started: 19 March 2026

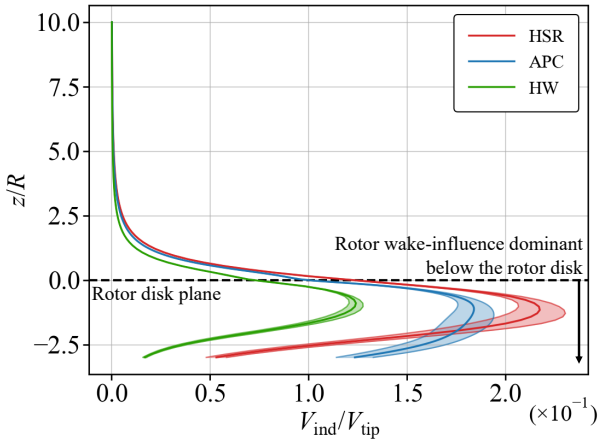

Figure A1. Comparison of time-averaged velocity magnitude normalized by V_{tip} plotted against normalized height z/R for three different rotors operating at nearly the same disk loading DL = 100 N/m^2 in hover.

collapse reasonably well, especially in the far wake region $(z/R < -3)$. The deviations observed in the near wake region $(-3 < z/R < 0)$ could be attributed to differences in the blade geometry – chord and twist distributions, tip shapes, thickness and taper; these differences can be observed to diminish with downstream distance, indicating the induced velocity field, when non-dimensionalized using the tip speed (V_{tip}), and analyzed in the non-dimensional axial frame z/R, is relatively independent of absolute rotor scale when operated under similar DL conditions.

Appendix B: Validation of the in-house FVM model

The current FVM implementation was validated for unsteady and steady flow conditions by the authors (Narayanan and Govindarajan, 2024), and the key results are summarized here. Three different validation scenarios (aside from the one presented in the main document; see Fig. 8) were considered

1. Power polar (thrust vs power) prediction for the full-scale Harrington single and coaxial rotors (Harrington, 1951) – steady flow
2. Rotor thrust and power prediction for varying angular speed (RPM) for the UAV-scale APC single-rotor (Brandt et al., 2015) – steady flow
3. Pitch rate study of the full-scale Carpenter–Fridovich single-rotor (Carpenter and Fridovich, 1953) – unsteady flow

B1 Harrington experiments

The Harrington single and coaxial rotor systems (Harrington, 1951) are 2-bladed, constant chord $(0.46\ \text{m})$, untwisted, full-scale helicopter rotors; the rotor radius (R) is 3.81 m, with an 18% R root cut-out length. The vertical separation between the

https://doi.org/10.5194/egusphere-2026-977
Preprint. Discussion started: 19 March 2026

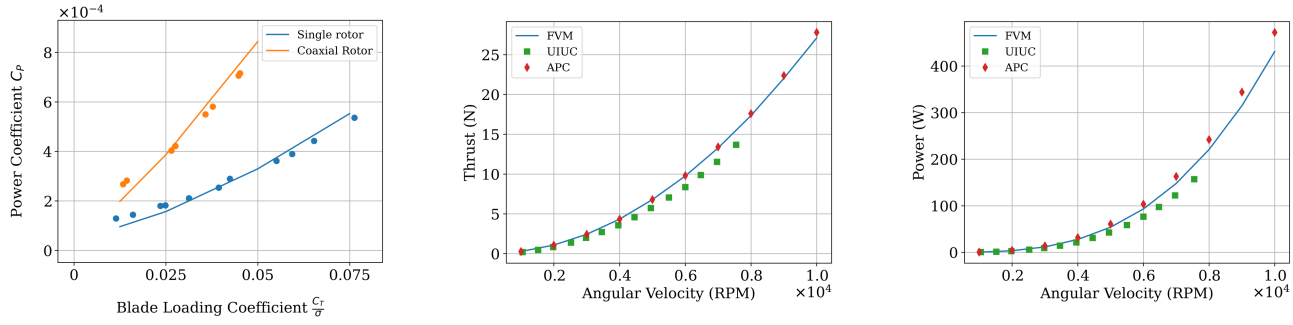

Figure B1. Validation of the developed FVM model for steady flow cases: **(a)** Harrington Polar Power; **(b)** APC, Thrust vs RPM; **(c)** APC, Power vs RPM.

rotors of the coaxial configuration is $20\%\ R$. The rotors from the original experiments were thickness-tapered along the span of the blade, while the current FVM implementation utilized a constant drag coefficient across the rotor, a strategy implemented in prior studies (Syal and Leishman, 2012). Figure B1a depicts the power polar for the Harrington single (blue) and coaxial rotors (orange). Blade loading coefficient (C_T/σ) is chosen as the independent parameter in place of rotor thrust, to emphasize the lift loading on the blades. The solid lines correspond to the FVM results, and the circular makers represent the original experimental results (Harrington, 1951). The single-rotor was operated at 200 RPM $(20.96\ \mathrm{rad s^{-1}})$ and the coaxial rotors were operated at 300 RPM $(31.36\ \mathrm{rad s^{-1}})$ across all the blade loading conditions, and the systems were trimmed to the target thrust, and zero in-plane moments by varying the rotor collectives. It can be observed that the FVM results predict the original experimental results with a significantly well, lending confidence in the developed FVM model; deviation in the results for lower thrust values could be attributed to the use of a constant drag coefficient in place of the tapered thickness rotor as in the original experiments.

B2 APC 12×6E single-rotor studies

The APC propeller is a UAV-scale 2-bladed rotor of radius $(R = 0.15\ \mathrm{m})$, with the root cut-out measuring $18.3\%\ R$. The spanwise chord and twist distributions of the rotor is detailed in a previous work by the authors (Narayanan and Govindarajan, 2024). The thrust and power variations against rotor RPM were studied for the APC single-rotor, as shown in Fig. B1b and Fig. B1c, respectively. NACA 0012 airfoil with a modified zero-lift angle of attack $(\alpha = -2°)$ and drag coefficient $(C_d = 0.012)$, was used as a surrogate to the actual airfoil sections used in the APC rotor. The fixed pitch APC rotor was treated as a rotor with a constant collective $(\theta_0 = 5°)$. It was observed that the FVM results were in good agreement with the UIUC and APC results (Brandt et al., 2015; APC Propellers, 2025) across all angular speeds (RPM), thereby validating the performance of the FVM model for steady problems for small-scale UAVs, in addition to the Harrington rotor problem.

https://doi.org/10.5194/egusphere-2026-977
Preprint. Discussion started: 19 March 2026

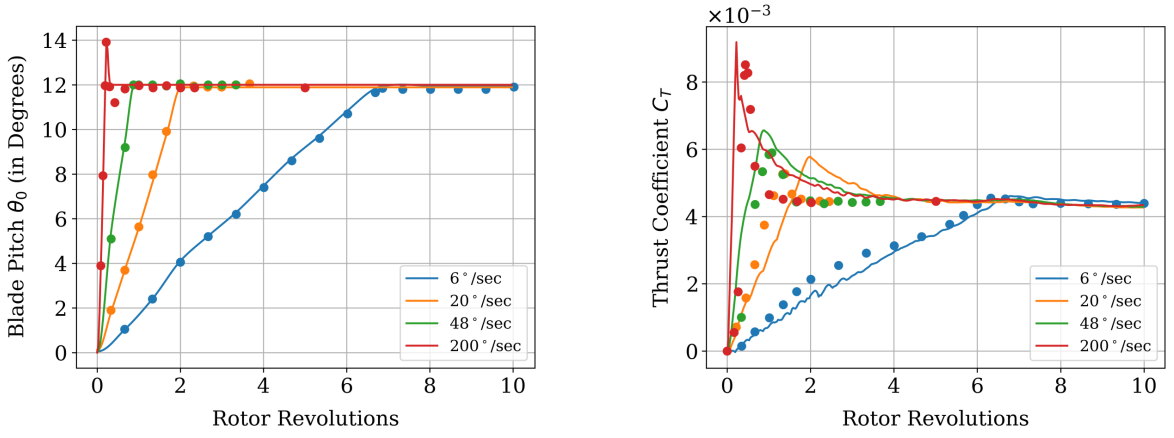

Figure B2. Validation of the developed FVM model for the unsteady flow case: **(a)** Time history of rotor blade pitch; **(b)** Time history of rotor thrust coefficient.

B3 Carpenter–Fridovich experiments

Carpenter–Fridovich experiments (Carpenter and Fridovich, 1953) were carried out to study the thrust response to rapidly pitching rotors. The rotor is a 2-bladed, untwisted, radius $R = 5.79$ m, full-scale helicopter rotor, with a root cut-out of 20% R, and constant chord of 0.25 m. To validate the FVM model for unsteady conditions, the pitch input from the original experiments were reproduced in the FVM model, for various pitch rates ($6°$ to $200°$ per second) to increase the blade pitch from from $0°$ to $12°$. The time history of the pitch rate input is shown in Fig. B2a. The highest pitch rate in Fig. B2a ($200°$ per second, red) indicates an overshoot in pitch, which occurred due to the torsional response in the original experimental setup. The numerical formulation did not include the effects of structural dynamics, and therefore, the pitch input was mimicked as in the experiment. It can be inferred from the thrust response of the system (Fig. B2b) that the FVM model captures the variation in thrust coefficient reasonably well in comparison to the original experiments, for all the pitch rates. For the highest pitch rate, the peak increase in the coefficient of thrust to nearly twice the steady state thrust value is also predicted well by the FVM model, adding to the reliability of the model in solving unsteady problems.

Data availability. The simulation data that support the findings of this study are available from the corresponding author upon reasonable request.

https://doi.org/10.5194/egusphere-2026-977
Preprint. Discussion started: 19 March 2026

Author contributions. Ashish Pastay: Investigation; Software; Formal analysis; Visualization; Writing — original draft; Writing — review and editing.
Shrivathsan Narayanan: Methodology; Investigation; Formal analysis; Writing — original draft; Writing — review and editing.
Bharath Govindarajan: Conceptualization; Methodology; Supervision; Formal analysis; Writing – review and editing.

Competing interests. The corresponding author has declared that none of the authors has any competing interests.

Disclaimer. None.

Acknowledgements. Figure 1 was enhanced using a generative artificial intelligence tool to improve visual clarity and presentation quality. The AI tool was used solely for graphical refinement and did not generate, modify, or influence any scientific content, data, interpretation, or conclusions presented in this study. All scientific content remains entirely the responsibility of the authors.

https://doi.org/10.5194/egusphere-2026-977
Preprint. Discussion started: 19 March 2026

References

Ananthan, S. and Leishman, J. G.: Role of filament strain in the free-vortex modeling of rotor wakes, J. Am. Helicopter Soc., 49, 176–191, https://doi.org/10.4050/JAHS.49.176, 2004.

APC Propellers: 12×6E Propeller Product Specifications, https://www.apcprop.com/product/12x6e/?v=c86ee0d9d7ed (last access: 18 February 2026), 2025.

Basawanal, A., Laliberte, J., Borshchova, I., and Traub, L.: Experimental study of an ultrasonic anemometer for drone-based measurements, Drone Syst. Appl., 1, 1-XX, https://doi.org/10.1139/dsa-2024-0035, 2025.

Bauknecht, A., Merz, C. B., Raffel, M., Landolt, A., and Meier, A. H.: Blade-tip vortex detection in maneuvering flight using the background-oriented schlieren technique, J. Aircraft, 51, 2005–2014, https://doi.org/10.2514/1.C032672, 2014.

Bhagwat, M. J. and Leishman, J. G.: Stability analysis of helicopter rotor wakes in axial flight, J. Am. Helicopter Soc., 45, 165–178, https://doi.org/10.4050/JAHS.45.165, 2000.

Bhagwat, M. J. and Leishman, J. G.: Accuracy of straight-line segmentation applied to curvilinear vortex filaments, J. Am. Helicopter Soc., 46, 146–155, https://doi.org/10.4050/JAHS.46.166, 2001.

Brandt, J. B., Deters, R. W., Ananda, G. K., Dantsker, O. D., and Selig, M. S.: UIUC Propeller Database, Version 3, University of Illinois at Urbana-Champaign, https://m-selig.ae.illinois.edu/props/propDB.html (last access: 18 February 2026), 2015.

Carpenter, P. J. and Fridovich, B.: Effect of a rapid blade-pitch increase on the thrust and induced-velocity response of a full-scale helicopter rotor, NACA Tech. Note TN 3044, National Advisory Committee for Aeronautics, https://ntrs.nasa.gov/citations/19930083686 (last access: 18 February 2026), 1953.

Cho, A., Kim, J., Lee, S., and Kee, C.: Wind estimation and airspeed calibration using a UAV with a single-antenna GPS receiver and Pitot tube, IEEE Trans. Aerosp. Electron. Syst., 47, 109–117, https://doi.org/10.1109/TAES.2011.5705663, 2011.

Datta, A., Johnson, W., and Chung, J.: Review of rotor loads prediction with the emergence of rotorcraft CFD, 31st European Rotorcraft Forum, Florence, Italy, 1–24, 2005.

Faber, J., Gerding, M., and Köpnick, T.: Acquiring high-resolution wind measurements by modifying radiosonde sounding procedures, Atmos. Meas. Tech., 16, 4183–4193, https://doi.org/10.5194/amt-16-4183-2023, 2023.

Fujiwara, M., Sun, B., Reale, A., Cimini, D., Larosa, S., Borg, L., von Rohden, C., Sommer, M., Dirksen, R., Maturilli, M., Vömel, H., Kivi, R., Ingleby, B., Kramer, R. J., Demoz, B., Madonna, F., Carminati, F., Lewis, O., Candy, B., Thomas, C., Edwards, D., Noersomadi, Shimizu, K., and Thorne, P.: Justification for high-ascent attainment for balloon radiosonde soundings at GRUAN and other sites, Atmos. Meas. Tech., 18, 2919–2955, https://doi.org/10.5194/amt-18-2919-2025, 2025.

Gasch, P., Kasic, J., Maas, O., and Wang, Z.: Advancing airborne Doppler lidar wind profiling in turbulent boundary layer flow – an LES-based optimization of traditional scanning-beam versus novel fixed-beam measurement systems, Atmos. Meas. Tech., 16, 5495–5523, https://doi.org/10.5194/amt-16-5495-2023, 2023.

Ghirardelli, M., Kral, S. T., Müller, N. C., Hann, R., Cheynet, E., and Reuder, J.: Flow structure around a multicopter drone: a computational fluid dynamics analysis for sensor placement considerations, Drones, 7, 467, https://doi.org/10.3390/drones7070467, 2023.

Ghirardelli, M., Kral, S. T., Cheynet, E., and Reuder, J.: SAMURAI-S: sonic anemometer on a multi-rotor drone for atmospheric turbulence investigation in a sling load configuration, Atmos. Meas. Tech., 18, 2103–2124, https://doi.org/10.5194/amt-18-2103-2025, 2025.

Harrington, R. D.: Full-scale-tunnel investigation of the static-thrust performance of a coaxial helicopter rotor, NACA Tech. Note TN 2318, National Advisory Committee for Aeronautics, https://ntrs.nasa.gov/citations/19930083001 (last access: 18 February 2026), 1951.

https://doi.org/10.5194/egusphere-2026-977
Preprint. Discussion started: 19 March 2026

HobbywingDirect: HF 2480 Propeller Product Specifications, https://www.hobbywingdirect.com/products/xrotor-2480-propeller (last access: 18 February 2026), 2025.

Hollenbeck, D., Nunez, G., Christensen, L. E., and Chen, Y. Q.: Wind measurement and estimation with small unmanned aerial systems using onboard mini ultrasonic anemometers, IEEE Int. Conf. Unmanned Aircraft Syst., Dallas, TX, USA, https://doi.org/10.1109/ICUAS.2018.8453418, 2018.

Inoue, J. and Sato, K.: Wind speed measurement by an inexpensive and lightweight thermal anemometer on a small UAV, Drones, 6, 289, https://doi.org/10.3390/drones6100289, 2022.

Jin, L., Ghirardelli, M., Mann, J., Sjöholm, M., Kral, S. T., and Reuder, J.: Rotary-wing drone-induced flow – comparison of simulations with lidar measurements, Atmos. Meas. Tech., 17, 2721–2737, https://doi.org/10.5194/amt-17-2721-2024, 2024.

Lee, H., Sengupta, B., Araghizadeh, M. S., and Myong, R. S.: Review of vortex methods for rotor aerodynamics and wake dynamics, Adv. Aerodyn., 4, 20, https://doi.org/10.1186/s42774-022-00111-3, 2022.

Leishman, J. G.: Fundamentals of rotor aerodynamics, in: Introduction to Helicopter Aerodynamics, 2nd ed., Cambridge Univ. Press, Cambridge, UK, 55–114, ISBN 978-0-521-85860-1, 2006.

Leishman, J. G.: Unsteady airfoil behavior, in: Introduction to Helicopter Aerodynamics, 2nd ed., Cambridge Univ. Press, Cambridge, UK, 423–524, ISBN 978-0-521-85860-1, 2006.

Leishman, J. G., Bhagwat, M. J., and Bagai, A.: Free–vortex filament methods for the analysis of helicopter rotor wakes, J. Aircraft, 39, 759–775, https://doi.org/10.2514/2.3022, 2002.

LI-COR Environmental: LI-550 TriSonica Mini Wind & Weather Sensor – Product Specifications, https://www.licor.com/products/trisonica/LI-550-mini (last access: 18 February 2026), 2025.

Meteomatics AG: MeteoDrones – Weather Drones: UAV-based Atmospheric Sensing Systems, https://www.meteomatics.com/en/meteodrones-weather-drones/ (last access: 18 February 2026), 2025.

Menapia Ltd.: MetSprite: UAV-based Atmospheric Measurement Platform, https://www.menapia.tech/metsprite-platform (last access: 18 February 2026), 2025.

Narayanan, S. and Govindarajan, B.: Effects of gust on the aerodynamics of multi-rotors, Phys. Fluids, 36, 127169, https://doi.org/10.1063/5.0243421, 2024.

Narayanan, S., Govindarajan, B., and Chandel, A.: Effect of gust on coaxial rotors using free vortex methods, in: Proceedings of the Vertical Flight Society 80th Annual Forum & Technology Display, Montreal, Canada, 14–16 May 2024, 1–22, https://doi.org/10.4050/F-0080-2024-1262, 2024.

Pindado, S., Cubas, J., and Sorribes-Palmer, F.: The cup anemometer, a fundamental meteorological instrument for the wind energy industry, Sensors, 14, 21418–21452, https://doi.org/10.3390/s141121418, 2014.

Ritvanen, J., O'Connor, E., Moisseev, D., Lehtinen, R., Tyynelä, J., and Thobois, L.: Complementarity of wind measurements from co-located X-band weather radar and Doppler lidar, Atmos. Meas. Tech., 15, 6507–6519, https://doi.org/10.5194/amt-15-6507-2022, 2022.

Romani, G. and Casalino, D.: Rotorcraft blade-vortex interaction noise prediction using the lattice–Boltzmann method, Aerospace Sci. Technol., 88, 147–157, https://doi.org/10.1016/j.ast.2019.03.029, 2019.

Simon, N., Piqué, A., Snyder, D., Ikuma, K., Majumdar, A., and Hultmark, M.: Fast-response hot-wire flow sensors for wind and gust estimation on UAVs, Meas. Sci. Technol., 34, 025109, https://doi.org/10.1088/1361-6501/ac9f5c, 2022.

Stoffelen, A., Pailleux, J., Källén, E., Vaughan, J. M., Isaksen, L., Flamant, P., Wergen, W., and Andersson, E.: The atmospheric dynamics mission for global wind field measurement, Bull. Am. Meteorol. Soc., 86, 73-87, https://doi.org/10.1175/BAMS-86-1-73, 2005.

https://doi.org/10.5194/egusphere-2026-977
Preprint. Discussion started: 19 March 2026

Syal, M. and Leishman, J. G.: Aerodynamic optimization study of a coaxial rotor in hovering flight, J. Am. Helicopter Soc., 57, 012004, https://doi.org/10.4050/JAHS.57.042003, 2012.

Thielicke, W., Hübert, W., Müller, U., Eggert, M., and Wilhelm, P.: Towards accurate and practical drone-based wind measurements with an ultrasonic anemometer, Atmos. Meas. Tech., 14, 1303–1318, https://doi.org/10.5194/amt-14-1303-2021, 2021.

T-Motor: AT3520 Long Shaft Brushless Motor Specifications, https://uav-en.tmotor.com/2019/Motors_0226/217.html (last access: 18 February 2026), 2024.

Wilson, T. C., Brenner, J., Morrison, Z., Jacob, J. D., and Elbing, B. R.: Wind speed statistics from a small UAS and its sensitivity to sensor location, Atmosphere, 13, 443, https://doi.org/10.3390/atmos13030443, 2022.

Witte, B. M., Singler, R. F., and Bailey, S. C. C.: Development of an unmanned aerial vehicle for the measurement of turbulence in the atmospheric boundary layer, Atmosphere, 8, 195, https://doi.org/10.3390/atmos8100195, 2017.

Zanotti, A., Savino, A., Palazzi, M., Tugnoli, M., and Muscarello, V.: Assessment of a mid-fidelity numerical approach for the investigation of tiltrotor aerodynamics, Appl. Sci., 11, 3385, https://doi.org/10.3390/app11083385, 2021.